ADVANCED OPTICAL MATERIALS
www.advopticalmat.de

Silver-Bismuth Based 2D Double Perovskites $(4FPEA)_4AgBiX_8$ (X = Cl, Br, I): Highly Oriented Thin Films with Large Domain Sizes and Ultrafast Charge-Carrier Localization

*Rik Hooijer, Andreas Weis, Alexander Biewald, Maximilian T. Sirtl, Julian Malburg, Rico Holfeuer, Simon Thamm, Amir Abbas Yousefi Amin, Marcello Righetto, Achim Hartschuh, Laura M. Herz, and Thomas Bein**

Two-dimensional (2D) hybrid double perovskites are a promising emerging class of materials featuring superior intrinsic and extrinsic stability over their 3D parent structures, while enabling additional structural diversity and tunability. Here, we expand the Ag–Bi-based double perovskite system, comparing structures obtained with the halides chloride, bromide, and iodide and the organic spacer cation 4-fluorophenethylammonium (4FPEA) to form the $n = 1$ Ruddlesden–Popper (RP) phases $(4FPEA)_4AgBiX_8$ (X = Cl, Br, I). We demonstrate access to the iodide RP-phase through a simple organic spacer, analyze the different properties as a result of halide substitution and incorporate the materials into photodetectors. Highly oriented thin films with very large domain sizes are fabricated and investigated with grazing incidence wide angle X-ray scattering, revealing a strong dependence of morphology on substrate choice and synthesis parameters. First-principles calculations confirm a direct band gap and show type Ib and IIb band alignment between organic and inorganic quantum wells. Optical characterization, temperature-dependent photoluminescence, and optical-pump terahertz-probe spectroscopy give insights into the absorption and emissive behavior of the materials as well as their charge-carrier dynamics. Overall, we further elucidate the possible reasons for the electronic and emissive properties of these intriguing materials, dominated by phonon-coupled and defect-mediated polaronic states.

1. Introduction

The exploration of 2D hybrid perovskites has gained increased attention, along with the success of their 3D analogs as optoelectronic materials for solar cells, laser diodes, and field-effect transistors, X-ray- and photodetectors or light-emitting diodes.[1–6] While a large number of 3D and 2D metal halide perovskites based on divalent metals such as Pb^{2+}, Sn^{2+}, Cu^{2+}, Mn^{2+}, Cr^{2+},and Cd^{2+} have been reported, a larger variety of materials based on the double perovskite structure $A^I{}_2B^IB^{III}X_6$ with A- and B-site cations and halides X remain comparatively uninvestigated. If not only the compositional variety of 3D double perovskites is considered, but also the dimensional reduction to 2D phases of such, the structural and compositional possibilities become phenomenally vast. By introducing mono- or multivalent organic A-site spacer cations, the materials' properties can be tuned by the variation of the spacer cation and also the thickness of the octahedral layers of the perovskite that are separated by the spacer cation.

R. Hooijer, A. Weis, A. Biewald, M. T. Sirtl, J. Malburg, R. Holfeuer, S. Thamm, A. A. Y. Amin, A. Hartschuh, T. Bein
Department of Chemistry and Center for NanoScience (CeNS)
University of Munich (LMU)
Butenandtstraße 5–13, 81377 Munich, Germany
E-mail: bein@lmu.de

The ORCID identification number(s) for the author(s) of this article can be found under https://doi.org/10.1002/adom.202200354.

DOI: 10.1002/adom.202200354

M. Righetto, L. M. Herz
Clarendon Laboratory
University of Oxford
Department of Physics
Oxford OX1 3PU, UK

L. M. Herz
Institute for Advanced Study
Technical University of Munich
Lichtenbergstrasse 2a, D-85748 Garching, Germany

Crystallographically speaking, a large number of double perovskites have been characterized or computed over the last 80 years, although the optoelectronic characterization and their potential for devices were only revisited recently.[7,8] Several halide double perovskites that are promising for optoelectronic application have been synthesized or computationally-predicted, such as $Cs_2AgBiCl_6$,[9] $Cs_2AgBiBr_6$,[5] Cu_2AgBiI_6,[10] $(MA)_2TlBiBr_6$ (MA = methylammonium),[11] $Cs_2AgSbCl_6$,[12] $Cs_2AgInCl_6$,[13] $Cs_2AgTlBr_6$,[14] $ASbCuX_6$ (A = monovalent cation, X = Cl, Br, I),[15] and $(MA)_2KBiCl_6$.[16]

The currently most studied double perovskite is $Cs_2AgBiBr_6$, mostly owing to its promising charge-carrier properties and its stability, despite its relatively large band gap of 2.0–2.3 eV.[17–22] Following this interest, more recently the effects of the dimensional reduction from 3D to 2D phases of $Cs_2AgBiBr_6$ have been reported by several groups by elaborating the theme in the form of $(BA)_4AgBiBr_8$, $(BA)_2CsAgBiBr_7$ (BA = butylammonium),[23] $(PEA)_4AgBiBr_8$ (PEA = phenethylammonium),[24–26] $(iPA)_2CsAgBiBr_7$ (iPA = isopentylammonium),[27] $(PA)_2CsAgBiBr_7$ (PA = propylammonium), $(PA)_4AgBiBr_8$, $(OCA)_4AgBiBr_8$ (OCA = octylammonium), and $(BDA)_2AgBiBr_8$ (BDA = 1,4-butyldiammonium).[28]

As a way of tuning the band gap of halide perovskites, it is known that changing the halide anion decreases its size in the order of $Cl^- > Br^- > I^-$.[29] The desirable double perovskite Cs_2AgBiI_6 is unfortunately not easily synthesized because of its negative decomposition enthalpy resulting in $CsAg_2I_3$ and $Cs_3Bi_2I_9$.[30,31] Another beneficial effect of the dimensional reduction is that the 2D phases of this silver bismuth iodide system are thermodynamically stable and compounds of the Ruddlesden–Popper (RP) n = 1 structure $(OC^I)_4AgBiI_8$ (OC^I = organic cation, monovalent; n = octahedral layer thickness) or the Dion-Jacobson n = 1 structure $(OC^{II})_2AgBiI_8$ (OC^{II} = divalent) were successfully synthesized and reported, thus enabling access to iodide double perovskites. Besides the reduced band gap energies around 2.0 eV caused by the heavier halide, a change in nature from indirect to direct band gap was reported several times to accompany the dimensional reduction from 3D to 2D systems.[23,32]

While bromide analogs have been reported with simple, alkylic, and aromatic spacer cations such as butylammonium or phenethyl ammonium, the iodide analogs have only been reported recently with more strongly interacting organic spacer cations, as, for example, divalent molecules forming Dion-Jacobson phases or molecules with an increasing number of ring systems, thus increasing the strength of aromatic interactions. Organic spacer cations with atomic interactions through terminating atoms such as iodine, as demonstrated for $(3IPA)_4AgBiI_8$ (3IPA = 3-iodopropylammonium), or fluorine (our work) have also shown this ability to stabilize the lattice of thermodynamically unfavored iodide phases.[33] For these, a sufficient templating effect through either structural rigidity or stronger molecular interactions is required to discourage the formation of more stable 0D or 1D Bi-I lattices.[34] For the choice of the organic spacer cation, ammonium-terminated alkylic or aromatic molecules are most commonly used, optionally with chain/ring-incorporation of nitrogen or sulfur atoms or halogen substitution at various hydrogen positions.[35–38]

Here, we synthesized three new compounds of the $(OC)_4AgBiX_8$ (X = Cl, Br, I) RP n = 1 structure with 4-fluorophenethylammonium (4FPEA) serving as the organic cation. We present the first comparative halide study for 2D double perovskites. The compounds were structurally and optoelectronically characterized in powder and thin film form. We synthesized single crystals of $(4FPEA)_4AgBiBr_8$ and $(4FPEA)_4AgBiI_8$ while for $(4FPEA)_4AgBiCl_8$ possible unit cell parameters were indexed. We use density-functional theory (DFT) to obtain insight into the electronic structure and atomic contributions to the frontier orbitals. Furthermore, we synthesized high-quality thin films and thoroughly characterized them by employing grazing-incidence wide angle X-ray scattering (GIWAXS). Finally, we provide initial insights into the charge-carrier dynamics and emissive properties, employing optical-pump terahertz-probe spectroscopy (OPTP) and photoluminescence (PL) measurements of these materials and incorporate them into photodetectors.

2. Results and Discussion

2.1. Structural Characterization

The 3D halide perovskite structure is based on the general formula ABX_3 with corner-sharing BX_6 octahedra, divalent metal cations B^{2+} and halide anions X^-, where monovalent A^+ cations occupy the cuboctahedral cavities. For the 3D double perovskite, the general formula is expanded to $A_2B^IB^{III}X_6$, following the same occupational rules with the difference that the corner-sharing octahedra are now alternating between B^IX_6 and $B^{III}X_6$. RP double perovskites with an octahedral layer thickness of n = 1 adopt the general formula $(OC)_4B^IB^{III}X_8$, where the organic cation (OC) replaces the A^+ cation and is also monovalent. The organic cations separate the octahedral layers, with the positively-charged group (i.e. NH_3^+) terminating into the cuboctahedral cavities, while the uncharged part interacts via van der Waals (v.d.W.) forces and dipole–dipole interactions, leaving a van der Waals gap between the organic layers.[39]

Investigating the structural properties of $(4FPEA)_4AgBiCl_8$, $(4FPEA)_4AgBiBr_8$, and $(4FPEA)_4AgBiI_8$ (synthesized from a simple solution approach explained in detail in the experimental part) we find very small changes, where the 4FPEA cation seems to have the dominant influence on the structural direction, enabling synthesis of the chloride and bromide structure but also stabilizing the iodide structure. In contrast, the unsubstituted phenethylammonium (PEA) cation can only yield the $(PEA)_4AgBiCl_8$ and $(PEA)_4AgBiBr_8$ compounds, but cannot stabilize the iodide structure (see XRD and EDX data in Figure S1, Supporting Information and Table S1, Supporting Information).

The structures of $(4FPEA)_4AgBiBr_8$ and $(4FPEA)_4AgBiI_8$ were determined through single-crystal X-ray diffraction, while for $(4FPEA)_4AgBiCl_8$ the lattice parameters were determined through indexing of powder XRD data. We note that the crystal structure of $(4FPEA)_4AgBiI_8$ was refined as a 2-component pseudomerohedral twin (pseudo-monoclinic cell) with a refined ratio of 0.75/0.25 for the two domains. The two equatorial iodides are slightly disordered with ratios of site

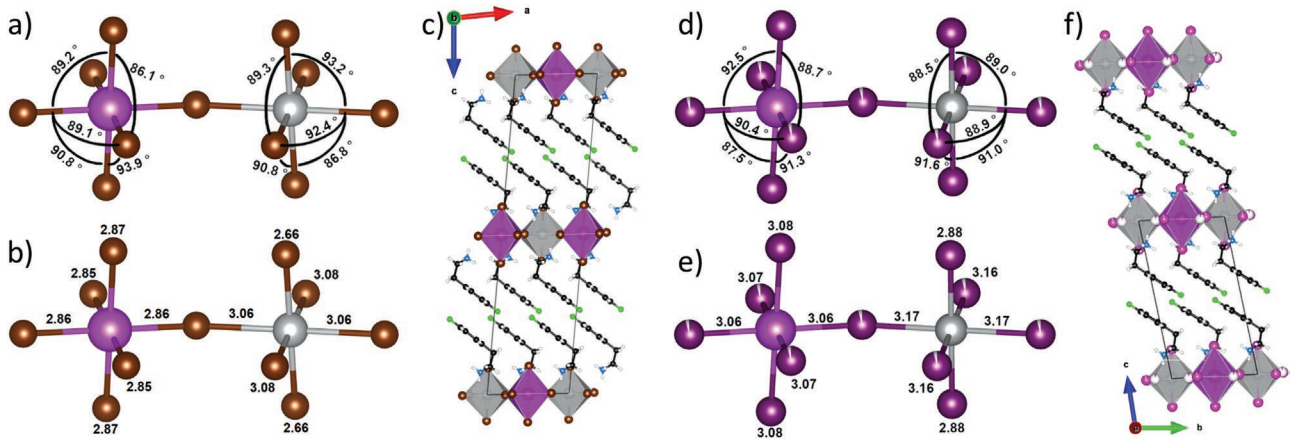

Figure 1. Single crystal structures of $(4FPEA)_4AgBiBr_8$ and $(4FPEA)_4AgBiI_8$ with a,d) octahedral angles in °, b,e) bond lengths in Å and c,f) comparative views of the unit cell of both structures. The bond angles shown are point symmetric with regard to their central metal atom and thus only shown once for clarity.

occupation factors refined to 0.97/0.03 as seen in Figure S2, Supporting Information. This disorder of equatorial iodines was also observed for other 2D iodide double perovskites such as $(AE2T)_2AgBiI_8$.[34] For the following comparative discussion, only the iodine sites with an occupation of 97% will be considered. Furthermore, we limit the discussion to the comparison of the crystal structures to the bromide and iodide analogs as seen in **Figure 1**.

Unlike the octahedra in the cubic $Cs_2AgBiBr_6$ that exhibit equivalent bond lengths (Bi–Br = 2.814 Å, Ag–Br = 2.821 Å) and metal-halide-metal angles of 90°, the octahedra in $(4FPEA)_4AgBiX_8$ are strongly distorted.[5] The angles in both structures in the Ag- and Bi-octahedra are equally distorted by up to 3.9° (Figure 1a,d). The bond lengths exhibit unequal distortion where the Ag-octahedra are strongly tetragonally contorted, resembling a Jahn–Teller effect with short axial bonds (Ag–Br = 2.66 Å, Ag–I = 2.88 Å) and long equatorial bonds (Ag–Br = 3.06/3.08 Å, Ag–I = 3.17/3.16 Å), while the Bi-octahedra are mostly symmetrically and only marginally distorted (Ag–Br = 2.85/2.86/2.87 Å, Ag–I = 3.06/3.07/3.08 Å) (Figure 1b,e). This tendency of monovalent Ag is also observed in compounds such as $Ag^{I}Ag^{III}O_2$, compounds with other similar d^{10} transition metals, e.g. Au^+ or Cu^+ or other recently reported, Ag-containing 2D hybrid double perovskites and is attributed to a mixing of filled transition-metal *n*d orbitals with empty $(n+1)$s orbitals, stabilizing a linear coordination geometry.[8,23,33,34,40,41]

One factor required to form 2D hybrid double perovskite iodides is the templating influence of the organic spacer cations, a term coined by Mitzi in 2000.[42] Both the RP and DJ phases require an in-plane interaction of suitably sized organic spacers to stabilize the 2D lattice, for example, aromatic, v.d.W. or dipole–dipole interactions. Contrarily, while the DJ phases have an intrinsically stronger interlayer connectivity by binding one organic layer to two adjacent inorganic layers through the divalent character, RP phases also require a strong interaction between organic spacer molecules along the out-of-plane direction. As of now, this synthetic difficulty has only yielded a small, but growing number of published structures, namely $(CHD)_2AgBiI_8 \cdot H_2O$ (CHD = 1,4-cyclohexandiamine),[43] $(AE2T)_2AgBiI_8$ (AE2T = 5,5′-diylbis(aminoethyl)-[2,2′-bithiophene]),[34] $(3AMPY)_2AgBiI_8$ (3AMPY = 3-(aminomethyl) pyridinium),[44] $(4AMP)_2AgBiI_8$ (4AMP = (4-(aminomethyl) piperidinium),[45] $(3IPA)_4AgBiI_8$ (IPA = 3-iodopropylammonium),[33] $(4IBA)_4AgBiI_8$ (IBA = 4-iodobutylammonium),[46] $(4AMP)_4AgBiI_8$,[47] $(APP)_4AgBiI_8$ (APP = 4-aminopiperidinium) and $(\beta\text{-MPA})_4AgBiI_8$ (β-MPA = β-methylphenethylammonium).[48] In our work, we used the simple modification of the PEA^+ cation to the $4FPEA^+$ cation to achieve the stabilizing and templating effect. To emphasize this, the structural differences between $(PEA)_4AgBiBr_8$ and $(4FPEA)_4AgBiBr_8$ are discussed in detail and shown in Figure S3, Supporting Information and Figure S4, Supporting Information.

Figure 2 shows the XRD patterns of polycrystalline powders and thin films of $(4FPEA)_4AgBiX_8$ (X = Cl, Br, I) as well as theoretical patterns based on the single-crystal structures of $(4FPEA)_4AgBiBr_8$ and $(4FPEA)_4AgBiI_8$. For $(4FPEA)_4AgBiCl_8$ a single crystal has not been obtained, but the indexed lattice parameters agree well with the powder XRD pattern and the lattice parameters of the bromide and iodide analog (Table S2, Supporting Information). For the bromide and iodide compounds, the experimental patterns also agree well with the simulated ones, without any detectable impurities, which we confirmed through a profile refinement (Figure S7, Supporting Information). Consistently, energy dispersive X-ray spectroscopy confirms the stoichiometric ratio for both crystals and thin films for all three compounds (Table S3, Supporting Information). A slight shift towards larger angles can be observed for both compounds from calculated to experimental diffractograms, indicating homogeneous lattice strain and thus a slightly compressed unit cell for experimental samples. From the thin film diffractograms, a strong orientation along the (00l) planes can already be observed, which is characterized more thoroughly with GIWAXS measurements (see below). If the three halide compounds are compared from Cl to Br to I, a shift toward smaller angles for the (hk0) planes can be observed, which is consistent with the increasing size of the unit cell in a and b directions, caused by the increase of ionic size of the halides and the increased equatorial metal-halide bond lengths (Table S2, Supporting Information). In contrast, the (00l) planes are shifted toward larger angles from Cl to Br to

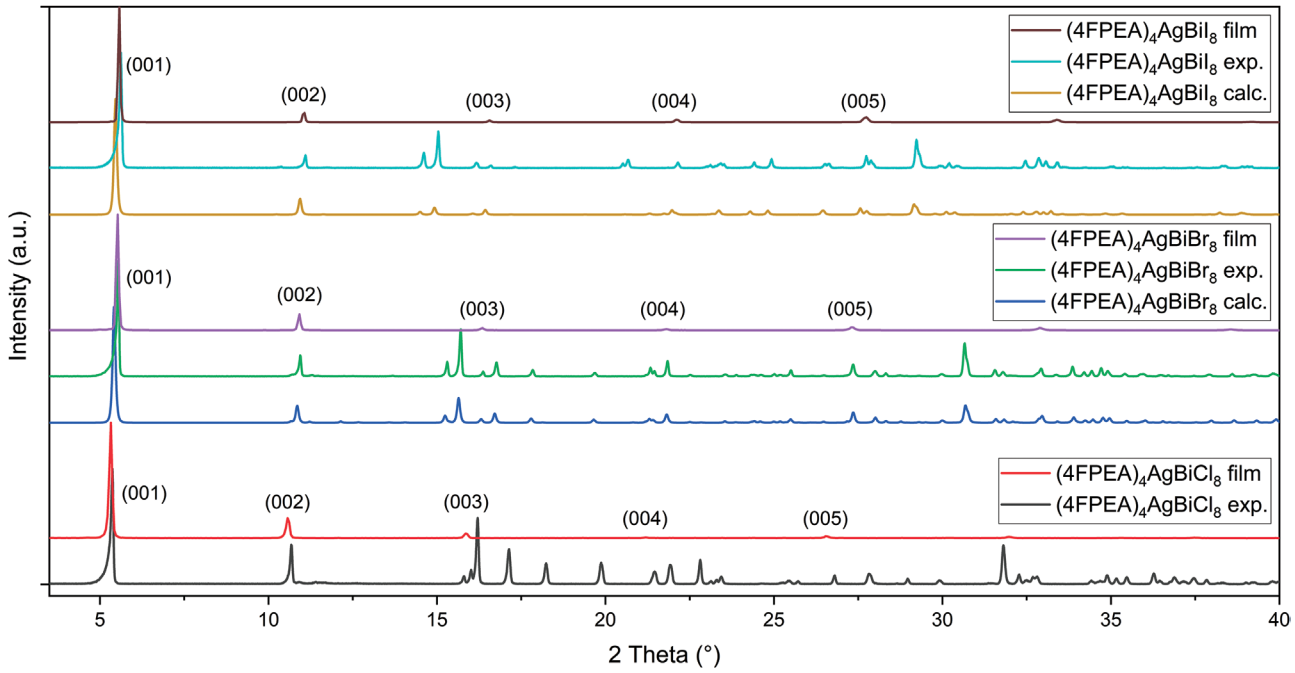

Figure 2. XRD patterns of thin films on ITO annealed at 140 °C and powdered crystals of $(4FPEA)_4AgBiX_8$ (X = Cl, Br, and I) grown in solution along with calculated patterns for $(4FPEA)_4AgBiBr_8$ and $(4FPEA)_4AgBiI_8$ derived from single-crystal structures.

I, also in agreement with the decrease of the unit cell size in the c direction. While the increase in bond distances and the ionic size is consistent for the axial octahedral bonds, the decrease in the c direction can be attributed to the slightly closer packing of the inorganic and organic layers.

2.2. Orientation and Thin Film Morphology

Thin films of $(4FPEA)_4AgBiCl_8$, $(4FPEA)_4AgBiBr_8$, and $(4FPEA)_4AgBiI_8$ were fabricated by spin coating from N-methyl-2-pyrrolidone (NMP) solutions onto different substrates with a subsequent annealing step. All three compounds in thin film form are strongly oriented along the (00l) planes, corresponding to a parallel orientation of inorganic and organic layers to the substrate surface. This horizontal orientation is typical for single-layered n = 1 2D double perovskite phases and so far, no other orientations have been prepared.[48,49] Furthermore, while for Pb- and Sn-based 2D perovskites higher n phases and vertical orientations have been reported, for Ag-Bi-based double perovskite systems $(BA)_2CsAgBiBr_7$, $(iPA)_2CsAgBiBr_7$ and $(PEA)_2CsAgBiBr_7$ remain the only known ones exhibiting the n = 2 thickness, though no thin films have been reported thus far.[23,26,27] While other studies have focused on initial thin film syntheses for n = 1 2D double perovskites,[33,34,43,47] here we have optimized the morphology of the thin films on different substrates and were able to observe structural differences depending on the choice of substrate roughness, the different halides, and annealing temperature.

To compare the influence of the substrate roughness we chose FTO-coated glass, ITO-coated glass, and Si–SiO_2 wafers as they are commonly used substrates for optoelectronic applications such as photovoltaics, photodetectors, light emitting diodes or field-effect transistors. The difference in surface roughness between these substrates is about one order of magnitude, with height differences (as RMS) of ±60 nm for FTO, ±5 nm for ITO, and ±1 nm for the polished SiO_2 wafer, see Figure S8, Supporting Information, for line profile scans and AFM images.

All thin film diffractograms exhibit the same general orientation along (00l) as shown in Figure 2 and **Figure 3**. We observe the same trends in crystallinity and an increasing quality from Cl > Br > I (a more detailed discussion of the diffractograms is given in the Supporting Information under Figure S9). One key feature is the splitting and broadening of reflections for the $(4FPEA)_4AgBiBr_8$ films, which we attribute to increased lattice parameters for higher annealing temperatures of 140 °C versus 100 °C, exerting tensile stress on the crystal lattice. To identify these different phases, a profile refinement revealed the slightly different lattice parameters for the concerned films, see Table S4, Supporting Information. Interestingly, while the annealing temperatures for all three substrates were identical, there is an observable difference in the diffractograms. We attribute this to the varying thickness and heat conductivity of the substrates. While the silicon wafer already has a higher heat conductivity than ITO and FTO coated glass substrates, additionally the substrate thickness increases from 0.625 mm (Si–SiO_2 wafer) to 1 mm (ITO coated glass) and 3 mm (FTO coated glass), which leads to a faster heat transfer along FTO < ITO < SiO_2. This results in a decreasing rate of solvent evaporation and crystallization toward FTO substrates. We believe this to be a reason why for FTO samples a mixture of both phases is seen for both temperatures, while for ITO the two phases are formed much more distinctly and on SiO_2 the crystallization is basically too fast for a distinct phase to form, leading to a broad reflection profile that indicates a

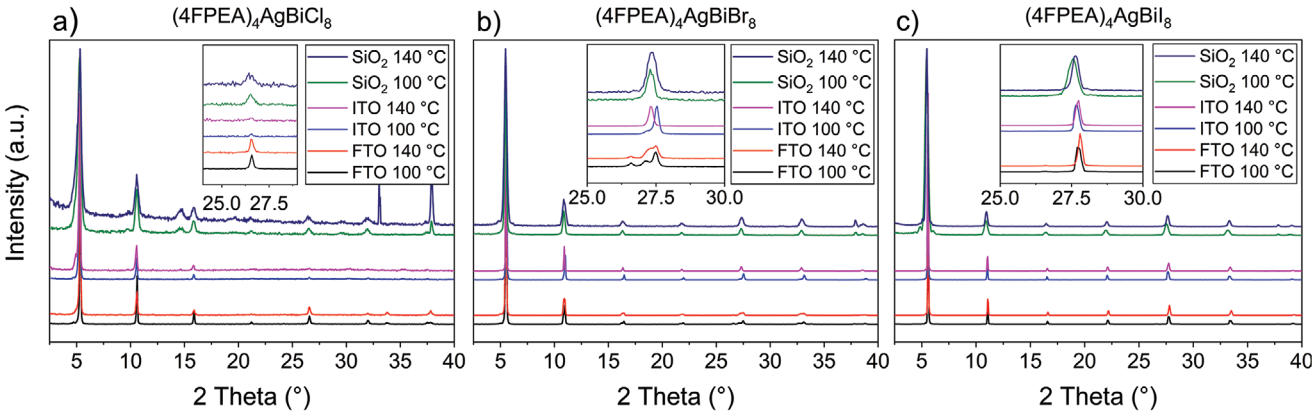

Figure 3. XRD patterns of thin films of a) $(4FPEA)_4AgBiCl_8$, b) $(4FPEA)_4AgBiBr_8$ and c) $(4FPEA)_4AgBiI_8$ on substrates FTO, ITO, and SiO_2 from NMP solution with annealing at 100 °C or 140 °C. The different parameters are indicated in the legends, insets show a magnified view of the 005 reflections.

very small crystallite size and a largely strained crystal lattice. Thin films of $(4FPEA)_4AgBiI_8$ show no additional reflections and no reflection splitting, as observed in $(4FPEA)_4AgBiBr_8$. Interestingly, the influence of the annealing temperature is inverse to that of $(4FPEA)_4AgBiBr_8$. With higher temperature the reflections shift toward higher angles compared to the diffractograms obtained with 100 °C annealing. This leads to the conclusion that while films of $(4FPEA)_4AgBiBr_8$ at 140 °C display increased lattice parameters and tensile stress, films of $(4FPEA)_4AgBiI_8$ show decreased lattice parameters and thus compressive stress. This trend is seen for all three substrates and while again the SiO_2-based films show broad reflections, they are also shifted toward higher angles.

To further analyze the influence of the substrate choice and annealing temperature, we performed GIWAXS measurements.

The films prepared on FTO substrates, having the roughest surface of the three substrates, show the largest broadening of the reflections along the azimuthal angle χ compared to a smaller broadening for ITO substrates and sharp reflection dots for SiO_2 substrates (**Figure 4**). This orientational degree can be visualized quantitatively by plotting the intensity of the 001 reflection with χ as the abscissa and is discussed in more detail under Figure S11, Supporting Information. The measurements shown in Figure S11, Supporting Information, reveal that for all films the orientation is present and of the same degree throughout the complete film. Only for $(4FPEA)_4AgBiCl_8$ and $(4FPEA)_4AgBiBr_8$ films on FTO the orientations show slightly larger FWHMs for the surface layers indicating a marginally smaller degree of horizontal orientation. Furthermore, if annealing temperatures are compared,

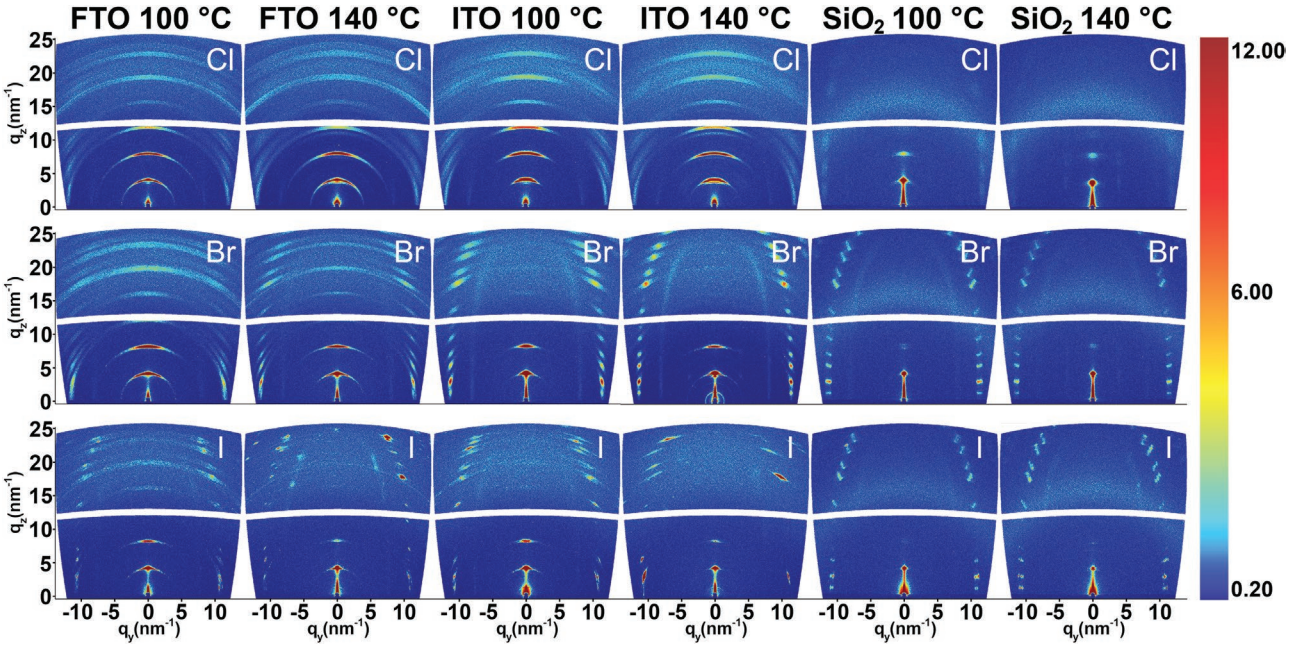

Figure 4. GIWAXS images of $(4FPEA)_4AgBiCl_8$, $(4FPEA)_4AgBiBr_8$, and $(4FPEA)_4AgBiI_8$ on FTO, ITO, and SiO_2 annealed at 100 °C and 140 °C, measured with an incident angle $\alpha_i = 0.2°$.

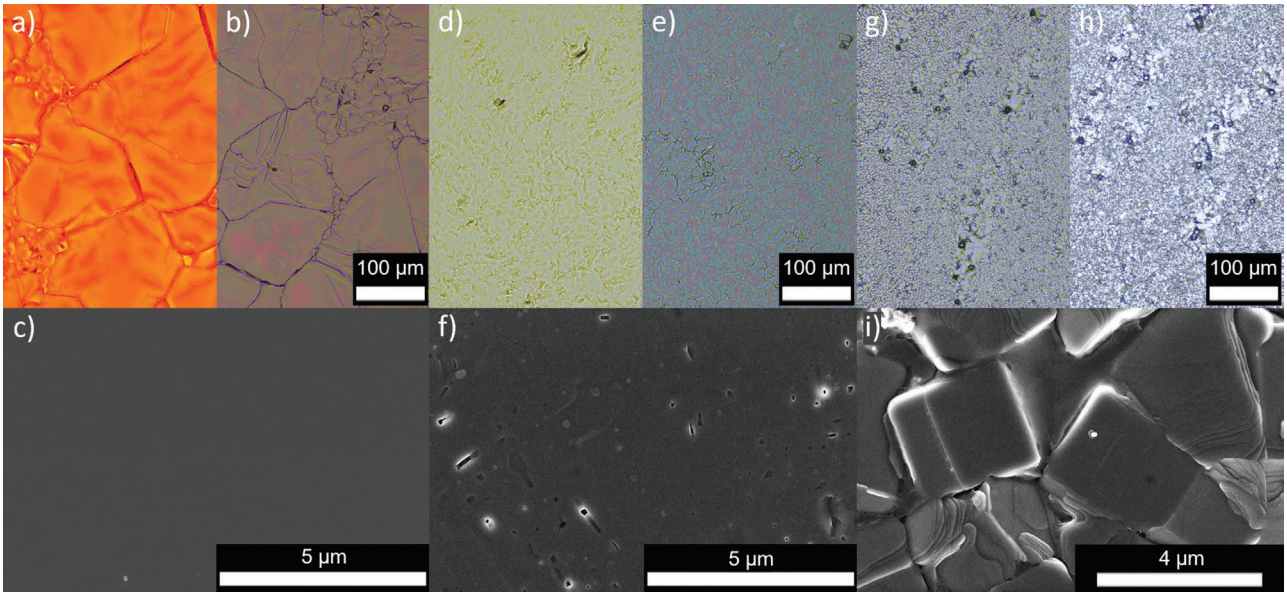

Figure 5. Optical microscopy (OM) images (top row) and SEM images (bottom row) for $(4FPEA)_4AgBiI_8$ a–c), $(4FPEA)_4AgBiBr_8$ d–f) and $(4FPEA)_4AgBiCl_8$ g–i). OM images are shown in transmission lighting on the left and illumination lighting on the right (top) for the respective compound.

140 °C compared to 100 °C results in sharper reflection spots and thus a higher degree of orientation. The main difference of these annealing temperatures is the increase in vapor pressure of the solvent N-methyl-2-pyrrolidone (NMP). With a boiling point of 202 °C, the vapor pressure increases almost tenfold from 3 kPa at 100 °C to 27 kPa at 140 °C, at ambient pressure.[50] This results in a much faster crystallization of the films, resulting in larger domains and a higher degree of orientation (Figure S13, Supporting Information). Finally, the crystallinity and degree of orientation increases for Cl < Br < I (Figure S14, Supporting Information). This can be seen by the decreased azimuthal broadening of reflections for Cl, Br, and I, respectively, as well as the increasing sharpness and intensity of reflections that originate from different (11l) planes, located at scattering vectors q_y = 10 and −10 nm^{-1} (Figure 4). For the chloride perovskites these reflections are only visible as weak and very broad areas, while for the bromide perovskites they are more distinct with an increased sharpness from FTO < ITO < SiO_2 and are distinctly shown as diffraction spots for the iodide. In the same way, the reflections of the 00l planes are only visible on FTO, while on ITO for the bromide and iodide the relative intensity of the 001 and 002 reflection is too high for reflections of l > 2 to be observable, demonstrating the high crystallinity of the $(4FPEA)_4AgBiBr_8$ and $(4FPEA)_4AgBiI_8$ thin films. This relative increase is seen again for films on the SiO_2 substrates where only the 001 reflection is observable. To confirm the orientation and assignment of diffraction planes, indexed 2D GIWAXS images of thin films annealed at 100 °C are shown in Figure S14, Supporting Information, for all three compounds confirming the crystal phase of the thin films. While the diffraction positions of (00l) planes agree well with the calculated positions, the diffraction positions of planes including *a* and *b* lattice parameters exhibit a shift indicating a compressed unit cell in *a* and *b*. This almost single-crystalline, excellent orientation of the iodide thin films achieved by a simple-solution-based spin-coating process is remarkable. A similar high level of orientation and near single-crystalline growth has been achieved very recently by Zhao et al. with $(R/S\text{-}\beta\text{-}MPA)_4AgBiI_8$ utilizing a strongly crystallization-guiding capillary-bridge assembly technique.[48]

The surface morphology was probed with optical and scanning electron microscopy and both methods confirm the high quality of the films and their orientation. For example, here we show films fabricated on ITO substrates with the same experimental conditions for all three halides in **Figure 5**. The films of $(4FPEA)_4AgBiI_8$ are homogeneous and form large domains with dimensions of up to 100 × 100 µm as shown in Figure 5a,b. The smooth surface morphology is of very high quality as seen in the SEM image in Figure 5 c, where the contrast is homogeneous over the complete surface and grain boundaries inside a single domain cannot be observed. $(4FPEA)_4AgBiBr_8$ also forms homogeneous films throughout the complete film surface (Figure 5d,e), yet does not form the large nearly perfect domains seen for the iodide perovskite. The domains seem bigger but rougher, which is also evident from the small holes in the SEM image in Figure 5f. Despite the small holes, the surface is still contrasted homogenously and grain boundaries cannot be observed. We note that for differently optimized parameters, an equally pristine surface can be obtained for $(4FPEA)_4AgBiBr_8$ films (Figure S15, Supporting Information). For $(4FPEA)_4AgBiCl_8$, the film quality is not as pristine as for the iodide or bromide structure. The OM images (Figure 5g,h) show a grained surface morphology and this is more clearly observable in the SEM image (Figure 5i) where single grains with dimensions in the range of several microns can be observed. Furthermore, the layered structure of the material can be clearly seen, as the individual layers stacking in the grains are evident for slightly tilted grains and with uneven surfaces.

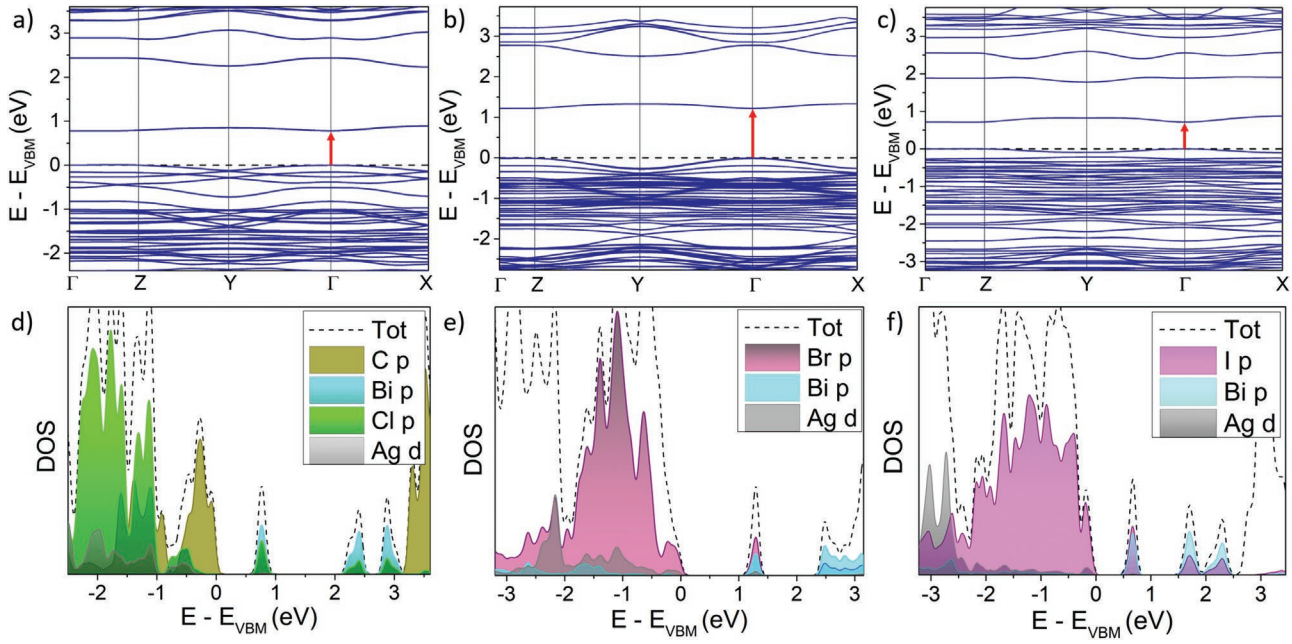

Figure 6. Band structures and projected density of states for a) and d) $(4FPEA)_4AgBiCl_8$, b) and e) $(4FPEA)_4AgBiBr_8$, and c) and f) $(4FPEA)_4AgBiI_8$. The direct transition at the Γ point is indicated as a red arrow in a), b) and c).

2.3. First Principles Calculations

To get insight into the electronic structure, DFT calculations were conducted. **Figure 6**a–c shows the PBE-SOC-TS band structures of $(4FPEA)_4AgBiX_8$ (X = Cl, Br, I). All calculations were carried out with the unit cells obtained from experimental single crystal data, although the band structure for $(4FPEA)_4AgBiCl_8$ was simulated starting from the iodide single crystal unit cell with the Rietveld refined unit cell parameters from the powder XRD measurements. The treatment of Bi-based 2D hybrid organic-inorganic perovskites with spin-orbit coupling (SOC) and dispersion correction is necessary to accurately describe the electronic structure in these materials as shown extensively in previous works.[23] The inclusion of spin-orbit effects leads to a splitting of the conduction band (CB), mostly consisting of Bi $6p_{1/2}$ orbitals (Figure 6d–f) in the CB. This was also shown prominently for the 3D compounds $Cs_2AgBiBr_6$ and $Cs_2AgBiCl_6$.[51] Furthermore, this conduction band separation leads to a change in the nature of the bandgap, centering the CB minimum at the Γ point as opposed to the X point as shown in Figure S17, Supporting Information, for the non-SOC case, leading to a direct transition for all compounds. This was suggested to arise from band back-folding because of the structural distortion in 2D double perovskites as demonstrated by Connor et al. and is a common phenomenon described in multiple theoretical simulations.[23,34] Furthermore, the degeneracy from Γ to Z highlights the reduced electronic dimensionality. The bandgaps in all calculations are under 2 eV, a significant and expected underestimation in comparison to the experimental results, mostly caused by the notorious ineffectiveness of DFT-PBE to quantitatively describe the experimental absorption edge values.[52]

To obtain insight into the atomic character of the frontier orbitals, the projected density of states (DOS) was evaluated for every compound. As expected, the character of the valence band maximum (VBM) and conduction band minimum (CBM) is similar for every halide, where the valence band (VB) consists of mostly halide-p and some Ag-d orbitals and the CB is predominantly made up of Bi-p and a contribution of halide p orbitals (analogous to Pb-p and I-p for 2D Pb systems),[53] in agreement with previous publications.[23,34] However, the VB character of $(4FPEA)_4AgBiCl_8$ seems to be of organic nature, with a dominant contribution of C-p states. Interestingly, the band dispersion appears to decrease from Cl to I, which we attribute to the growing degeneracy and separation of the organic HOMO and inorganic VB (Figure S18, Supporting Information), where the organic frontier orbital is almost isoenergetic to the inorganic component for I, further apart for Br and well separated for Cl. The compounds therefore mostly form type Ib heterojunctions between inorganic and organic quantum wells, except the chloride phase, which manifests type IIb behavior, but considering the limits of DFT simulations the iodide phase could also represent a IIb heterojunction as shown for $[AE2T]_2AgBiI_8$ by Jana et al.[34]

2.4. Optical Properties

2.4.1. Absorption

We employed UV–vis spectroscopy to determine the experimental values for the band gap energies for both powders and thin films. As the first principle calculations revealed the direct nature of the band gap, the Tauc plots for a direct allowed transition are shown as insets in **Figure 7** for *a*, thin films and *b*, powders. For thin films, a corrected absorption was calculated by measurement of transmittance and reflectance spectra according to Figure S21, Supporting Information. For powders,

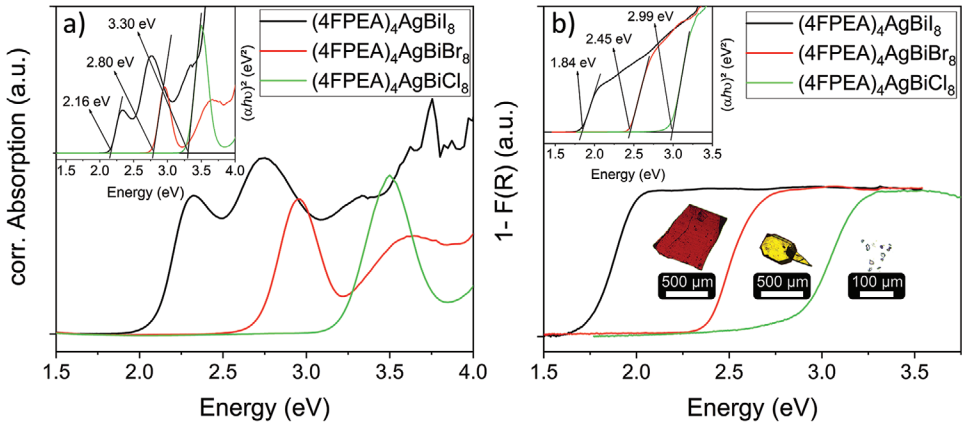

Figure 7. UV-vis absorption measurements with insets showing Tauc plots for a direct allowed transition for a) thin film and b) powder samples of $(4FPEA)_4AgBiI_8$, $(4FPEA)_4AgBiBr_8$, and $(4FPEA)_4AgBiCl_8$. Pictograms in b) show single crystals of the corresponding samples of $(4FPEA)_4AgBiI_8$ (left), $(4FPEA)_4AgBiBr_8$ (middle) and $(4FPEA)_4AgBiCl_8$ (right).

diffuse reflectance spectra were measured and transformed according to the Kubelka–Munk function $F(R)$.[54] The absorption and absorbance spectra show the typical blueshift for halide compounds with decreasing atomic number of the halide. The values for powders are 1.84, 2.45, and 2.99 eV and for thin films 2.16, 2.80, and 3.30 eV for $(4FPEA)_4AgBiI_8$, $(4FPEA)_4AgBiBr_8$ and $(4FPEA)_4AgBiCl_8$, respectively.

The lowest energy absorption in thin films is an isolated feature centered at 2.34 eV (iodide), 2.98 eV (bromide), and 3.53 eV (chloride). This feature is in line with other findings, as a strong isolated absorption maximum is also found for thin films of the 3D analog $Cs_2AgBiBr_6$ or 2D analogs like $(BA)_4AgBiBr_8$ or $(AE2T)_2AgBiI_8$.[23,49,55] The feature is rather broad, in line with the aforementioned analogs and in contrast to the observed sharp excitonic feature in lead-based 2D perovskites.[56] The broad character, the absence of a strong temperature dependence and the large exciton binding energy (EBE) attracted attention to the origin of this feature for $Cs_2AgBiBr_6$, and recently Wright et al. provided support for the theory that the absorption peak in the 3D compound arises from a direct exciton despite the mentioned anomalies.[55] A second isolated feature is visible at higher energies of 2.76 eV (iodide) and 3.66 eV (bromide) but overlapping with the UV absorption of the substrate and hence not measurable for the chloride. The second feature appears stronger for the iodide than for the bromide, being the absorption maximum at high energy blue light. This second feature is slightly less visible for the bromide and again not measurable for the chloride, due to the UV absorption overlap of glass. Furthermore, the simulated absorption from the dielectric response for the bromide reveals strikingly similar features, excluding excitonic effects (Figure S20, Supporting Information). Here, the two first absorption maxima are attributed to the inorganic contribution in the VBM and CBM, probably caused by the aforementioned Bi 6p band splitting.[57] Moreover, a similar mechanism as described by Jana et al. is suggested, where the absorption is traced back to the equatorial halide ion rather than a direct Ag to Bi transition, as the contributions of Bi p/Ag d in the VBM/CBM are negligible.[34] The intense lowest-energy absorption peak has also been demonstrated theoretically for inorganic and hybrid double perovskites A_2SbCuX_6, with the iodide compounds showing the highest maxima compared to lighter halide compounds. This absorption thus seems intrinsic to the double perovskite halide family.[15]

The powder absorption data display a redshift for all three compounds and do not show the distinct absorption features of the thin films as clearly, but still visible upon scaling (Figure S21, Supporting Information). The features, ordered from lower to higher energy, have their maxima for the iodide at 2.14, 2.39, 2.52, and 2.96 eV, for the bromide at 3.07 eV and for the chloride at 3.45 eV. The number of maxima match those of their respective thin film plots, although not as distinctly visible (for the iodide the feature at 2.14 eV appears very small, whereas the maxima at 2.39, 2.52, and 2.96 eV appear reminiscent of the observed pattern in the thin films, with the features at 2.39 eV and 2.52 eV either overlapping, which could be caused by the 2nd and 3rd CBM, or appearing due to low measurement resolution.) The shift of 0.32 eV (iodide), 0.35 eV (bromide), and 0.31 eV (chloride) relative to thin film data might be caused by anisotropic absorption, considering the rough surface of the powder and the resulting surface scattering, which is relevant to the variation in particle size of the powder, as well as the thickness dependence where indirect transitions in bulk powder measurements are statistically more relevant than for thin films of a few hundred nanometers.

2.4.2. Charge-Carrier Dynamics and Emission

In the following, we discuss the charge-carrier dynamics and emissive behavior of thin films of $(4FPEA)_4AgBiBr_8$ and $(4FPEA)_4AgBiI_8$. While these processes and the excitonic character of 3D $Cs_2AgBiBr_6$ are well established in the literature, they are yet to be fully explored for the 2D submembers of the double perovskite. Although substantial advances have been made recently by Schmitz et al. and Pantaler et al. elucidating the emissive features and charge-carrier dynamics of Ag–Bi–Br based 2D double perovskites, a comprehensive view is still lacking.[26,49,55,57,58] Here, we observe similarities owing to the related Ag-Bi double perovskite system, but also some differences between the perovskites with halides bromide and iodide.

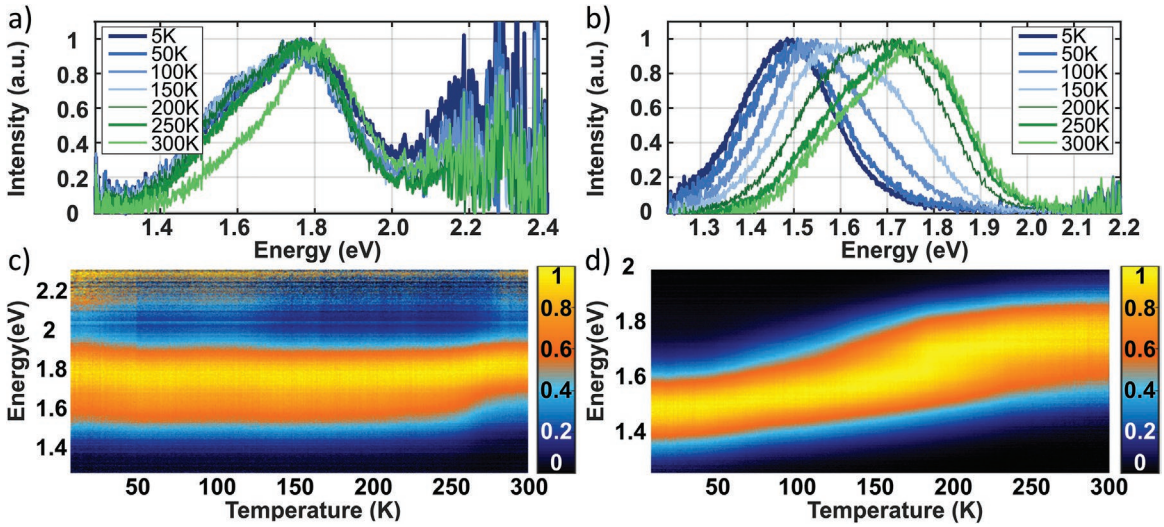

Figure 8. Temperature-dependent PL spectra and color plots of the normalized PL spectra at temperatures between 5 and 300 K for a) and c) $(4FPEA)_4AgBiBr_8$, and b) and d) $(4FPEA)_4AgBiI_8$.

Photoluminescence: Photoluminescence (PL) measurements on thin films show weak intensities and very broad emissions with a FWHM (full width half maximum) of 300 meV for the iodide and 320 meV for the bromide at room temperature (**Figure 8**a,b). The characteristic broad emission for these systems is also observed in other 2D silver-bismuth-halide, 2D lead-halide and 3D silver-bismuth-halide systems.[23,45,49,55,59] In $Cs_2AgBiBr_6$, it is generally attributed to substantial electron-phonon coupling, leading to self-trapping or localization of the charge carriers or excitons. These self-trapped charge carriers subsequently diffuse to color centers and recombine, leading to the broad and strongly red-shifted PL.[26,55,60]

Intriguingly, for $(4FPEA)_4AgBiI_8$ a significant spectral shift of the emission with decreasing temperature is observed, with a redshift of the emission maximum from 1.7 eV at 300 K to 1.46 eV at 5 K (Figure S22, Supporting Information). This is remarkable as this large shift is not observed in $Cs_2AgBiBr_6$ or other 2D silver-bismuth-halide double perovskites for which the temperature-dependent PL data have been examined.[34,55] While initially often argued that the broadness of the emission and thus the absence of a narrow emission at low temperatures is counterintuitive of a dominant excitonic contribution, we find a moderate reduction of the FWHM by 120 meV, from 320 meV at 300 K down to 200 meV at 5 K (Figure S22, Supporting Information). One reason for the persistent broadness of the PL is attributed to defect-mediated charge-carrier recombination and thus a considerable defect population. Since an intrinsic defect population has been reported for single crystals of $Cs_2AgBiBr_6$, demonstrating a tendency towards disorder and/or crystallographic imperfections arising from B-site metal disorder between Ag and Bi, we would assume this tendency of double perovskites to also be present in their 2D subsets.[17,60] Adding the fact that we measured thin film samples, with a rapid crystallization mechanism compared to a single crystal synthesis, we can assume an even higher number of defects, potentially explaining the large temperature-independent inhomogeneous broadening parameter $\Gamma_0 = 200$ meV (ignoring scattering from ionized impurities).[60,61] Contrary to these two trends observed for the temperature-dependent emission of $(4FPEA)_4AgBiI_8$, the emission for $(4FPEA)_4AgBiBr_8$ peak shifts only slightly, from 1.78 eV at 300 K to 1.68 eV at 5 K. On the other hand, the FWHM of the emission increases from 300 meV at 300 K up to 420 meV at 5 K. However, by inspecting more closely the PL temperature-dependent lineshape, we notice that the emergence of a lower energy feature (peaked at 1.6 eV) may conceal any spectral broadening and shifts of the peak observed at room temperature.

Interestingly, for $(PEA)_4AgBiBr_8$ a similar emission shape was observed for spectra recorded at 300 and 80 K, with a redshift or an emerging feature at lower energies 80 K.[26] We further notice a difference between the reported absorption with its maximum at 3.2 eV and our measurement with its absorption maximum at 3 eV. Such prominent Stokes shifts are also commonly reported for $Cs_2AgBiBr_6$, where exact values can depend on the measurement technique, as well as potentially on the morphology of the measured thin films (See Figure S16, Supporting Information, showing the flat and homogeneous surface morphology observed for the samples, compared to the dendritic or needle-shaped morphology of $(PEA)_4AgBiBr_8$ thin films reported in[26]).

In the following, we compare the PL data collected as part of our study of $(4FPEA)_4AgBiBr_8$ and $(4FPEA)_4AgBiI_8$ with the available data reported in the literature for $(PEA)_4AgBiBr_8$,[26] $(BA)_4AgBiBr_8$,[49] and $(iBA)_4AgBiBr_8$.[49] While the excitation energies and the reported PL ranges differ depending on the employed setup and the publication, they share similar overall features. Schmitz et al. proposed a sound explanation for the processes of the excited states,[49] which we confirmed and displayed schematically in **Figure 9**. Initially, at sufficient above band gap excitation free charge carriers are generated. Owing to the strong excitonic interactions in these materials, a fraction of the free carriers (depending on the EBE, usually in the hundreds of meVs for these materials) will rapidly form a free exciton state. Furthermore, because of the strong

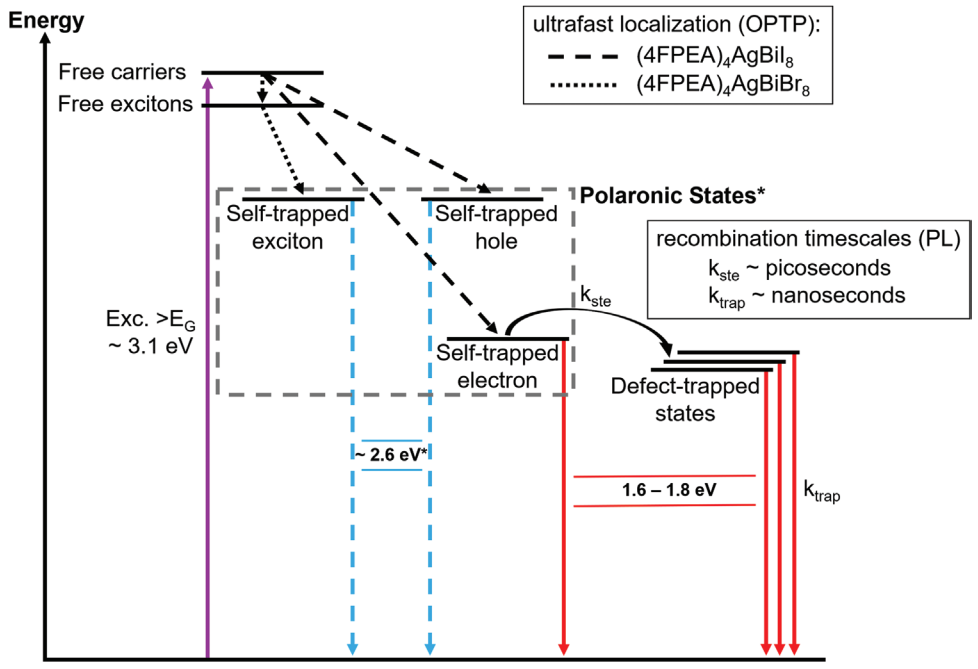

Figure 9. Schematic mechanism of the charge-carrier dynamics and emission for Ag-Bi based 2D double perovskites with exemplary energy values from our experiments, i.e. excitation energy of 3.1 eV and observed photoluminescence at around 1.6 eV. * The asterisk indicates the part of the model which was combined from previous findings in the literature on Ag-Bi-Br based 2D double perovskites and the reported energy ranges, i.e. emission at 2.6 eV from self-trapped excitons and self-trapped holes (not observable here due to the experimental setup) and emission at 1.6 – 1.8 eV from self-trapped-electrons and defect-trapped states. The PL data for $(4FPEA)_4AgBiI_8$ suggest that emission is dominated by intrinsic recombination, while for $(4FPEA)_4AgBiBr_8$ the emission is dominated by defect-mediated recombination (see amplitude ratios in figure S23, Supporting Information).

carrier-phonon interactions prevalent in these systems, these free charge carriers or free excitons subsequently undergo an ultrafast localization process or self-trapping forming a small polaron state. Moreover, these polarons will diffuse to color centers where recombination occurs.

To further complement these interpretations, we draw attention to the DFT studies reported by Schmitz et al.[49] These first-principle calculations on $(PEA)_4AgBiBr_8$ suggest that the PL emission energies of the differently trapped excited states vary substantially, in good agreement with their experimental observations. Namely, for the Ag–Bi–Br based materials, which feature the main absorption around 3 eV, they predicted the first, higher-energy emission at around 2.6 eV to be caused by either band-to-band exciton recombination or self-trapped hole recombination. The second, lower-energy emission at around 1.8 eV could be assigned to self-trapped electron or defect-mediated recombinations. Owing to our excitation energy of 3.06 eV for the PL measurements, being barely resonant with the main band gap absorption of $(4FPEA)_4AgBiBr_8$ at room temperature, as well as our detection limit at 2.1 eV, such high-energy emission was not observable. Nonetheless, the observed low-energy emission at 1.8 eV agrees well with the findings for the other Ag–Bi–Br systems. To explain the small redshift and the possible appearance of a second emissive feature at 1.6 eV with decreasing temperatures further research is still needed. Although the excitation energy of 3.06 eV should be sufficiently above the band gap absorption for $(4FPEA)_4AgBiI_8$, we are still limited with a detection limit at 2.1 eV, but the observed emission with its maximum at 1.7 eV is in line with the expected energies for self-trapped electron or defect-mediated recombination. The origin of the seemingly single feature with its much larger redshift with decreasing temperature could be due to the more dominant intrinsic recombination of the polaronic states, compared to the more defect-dominated recombination of the bromide.

We measured similar PL transients for both materials and fitted them with a biexponential decay function, which helped us identify two recombination processes occurring on different timescales. For $(4FPEA)_4AgBiI_8$ we report a first very short-lived component with lifetimes in the range of 20 ps at 300 K increasing to 100 ps at 5 K. The second, longer-lived component showed lifetimes of 1 ns at 300 K increasing to 50 ns at 5 K. The transients for both compounds are shown in Figure S23, Supporting Information. In the given model, we would assign the first, short lifetime to a charge hopping process of the self-trapped electrons from a slightly higher energy level before they fall into defect trap states, which can be confirmed by time- and spectral-dependent measurements, as shown in Figure S24, Supporting Information. For the energetically higher-lying spectral part above 1.7 eV, we find a higher amplitude ratio for the short-lived component compared to the energetically lower lying contribution below 1.3 eV. As the thermal barrier relatively increases at lower temperatures, this trap-mediation becomes less likely, self-trapped electrons live longer and thus the lifetime of the emission of self-trapped electrons increases. Additionally, we used an Arrhenius plot to extract an activation energy of 126 meV for $(4FPEA)_4AgBiBr_8$ and 20 meV for $(4FPEA)_4AgBiI_8$ as the energy barrier of said hopping process

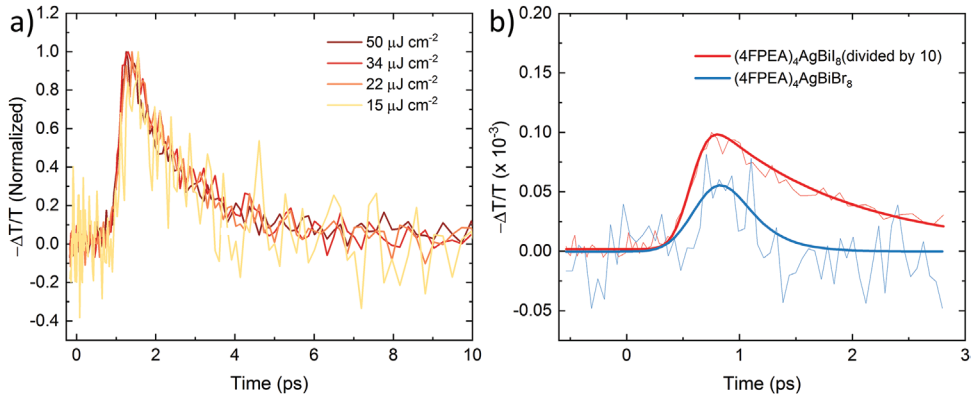

Figure 10. (a) Early time fluence-dependent optical pump terahertz probe (OPTP) signal measured for $(4FPEA)_4AgBiI_8$ after 3.1 eV pulsed excitation and fitted with a two-level mobility model, with the fits shown as colored solid lines. The two-level mobility model is explained in detail in the Supporting Information section (see Figure S28, Supporting Information). (b) Comparison between early time OPTP signal measured for $(4FPEA)_4AgBiI_8$ and $(4FPEA)_4AgBiBr_8$ after 3.1 eV pulsed excitation at a fluence of 50 μJ cm^{-2}. The signal for $(4FPEA)_4AgBiI_8$ is divided by a factor of 10 to facilitate the comparison. Solid lines represent experimental data and dashed lines represent fits to the two-level mobility model, described in the Supporting Information section (see Figure S28, Supporting Information).

(Figure S25, Supporting Information). The second, longer-lived lifetime component is assigned to defect-mediated recombination, which freezes out below temperatures of 100 K.

Optical-Pump Terahertz-Probe Spectroscopy: To further support the photophysical picture presented in Figure 9, we measured the early-time dynamics of photoexcited charge carriers for $(4FPEA)_4AgBiI_8$ and $(4FPEA)_4AgBiBr_8$ thin films by using optical-pump terahertz-probe (OPTP) spectroscopy. This technique monitors the dynamics of free charge carriers by measuring the change in transmitted THz electric-field amplitude (expressed here as $-\Delta T/T$) upon photoexcitation of the material using a 3.1 eV femtosecond laser pulse.

OPTP measurements for $(4FPEA)_4AgBiI_8$ (**Figure 10**a) reveal an ultrafast and almost complete decay of the photoconductivity within 10 ps after photoexcitation. Crucially, the observed photoconductivity signal is proportional to three factors: the photon-to-charge branching ratio ϕ (i.e., the fraction of free carrier density generated per absorbed photon density), the number of photogenerated charge carriers n and the electron-hole sum-mobility μ.[62] Therefore, in principle, the observed ultrafast decay can be caused by variations in each of these quantities, in processes such as exciton formation, charge carrier localization and defect-mediated recombination. The reported EBEs for 2D and 3D silver-bismuth halide perovskites are in the hundreds of meVs (250 meV for $(OC)_4AgBiI_8$ and ≈300 meV for $Cs_2AgBiBr_6$),[26,55] thus we expect strong excitonic interactions for thermally equilibrated charge carriers. However, we note that: i) at the typical excitation densities of OPTP experiments (≈10^{13} cm^{-2}), the Saha equation predicts a nonnegligible fraction of free carriers for EBEs > 200 meV;[63] and ii) the excess energy provided by 3.1 eV pump pulses implies the transient generation of free carriers rather than excitons.

Recent studies on $Cs_2AgBiBr_6$ and Cu_2AgBiI_6 reported a similar ultrafast decay of the photoconductivity and attributed this to the strong carrier-phonon coupling and the formation of small polarons, i.e., to an ultrafast localization of the charge carriers caused by a significant distortion of the lattice.[55,64] To test this hypothesis, we fitted the fluence-dependent OPTP data with a two-level mobility model developed by Wright and coworkers (explained in details in the SI, Supporting Information).[55] The excellent agreement between experimental data and fits supports the hypothesis of ultrafast carrier localization as a major cause in the ultrafast decay of photoconductivity. Furthermore, the fluence-independent nature of the OPTP signal (Figure S27, Supporting Information) rules out exciton formation as a possible cause.

The average initial mobility value for $(4FPEA)_4AgBiI_8$ extracted across the range of fluences is $\varphi\,\mu_{del} = 0.6 \pm 0.1$ cm^2 V^{-1} s^{-1}, almost five times lower than what was reported for $Cs_2AgBiBr_6$,[55] and the observed localization rate is $k_{loc} = 0.7 \pm 0.1$ ps^{-1}. Interestingly, the mobility after localization is below our detection limit and is set to zero in the fitting procedure. We note here that the OPTP sensitivity is in the range of $\mu \sim 0.1$ cm^2 V^{-1} s^{-1}. Therefore, our measurements reveal that the mobility after localization is < 0.1 cm^2 V^{-1} s^{-1}.[65] The observation of this low mobility supports the predictions of low electronic dimensionality for silver-bismuth halide elpasolites, which extended to bi-dimensional layers implies the complete electronic de-coupling of $[AgX_6]^{5-}$ and $[BiX_6]^{3-}$ octahedra (i.e., holes are localized on $[AgX_6]^{5-}$ octahedra, which are surrounded by $[BiX_6]^{3-}$ octahedra, thus hindering the charge-carrier hopping – and vice-versa for electrons).[66,67]

As shown in Figure 10b, the comparison between $(4FPEA)_4AgBiI_8$ and $(4FPEA)_4AgBiBr_8$ reveals a significantly reduced photoconductivity for the bromide counterpart. The estimated carrier mobility for $(4FPEA)_4AgBiBr_8$ is $\varphi\,\mu \approx 0.06$ cm^2 V^{-1} s^{-1} and the observed signal decay is almost limited by the time resolution of our setup (≈290 fs). Here, the lower branching ratio-times-mobility factor could be, in principle, caused by either a lower mobility or by a more prominent role played by excitons. We note that a comparatively lower excess energy is provided by the pump pulse (i.e., at 3.1 eV, $(4FPEA)_4AgBiBr_8$ is excited almost directly on its absorption peak). Furthermore, we also note that no substantial change of mobility or carrier-phonon coupling has been observed for 3D $Cs_2AgBiBr_6$ and Cu_2AgBiI_6 (i.e., different halides).[55,64]

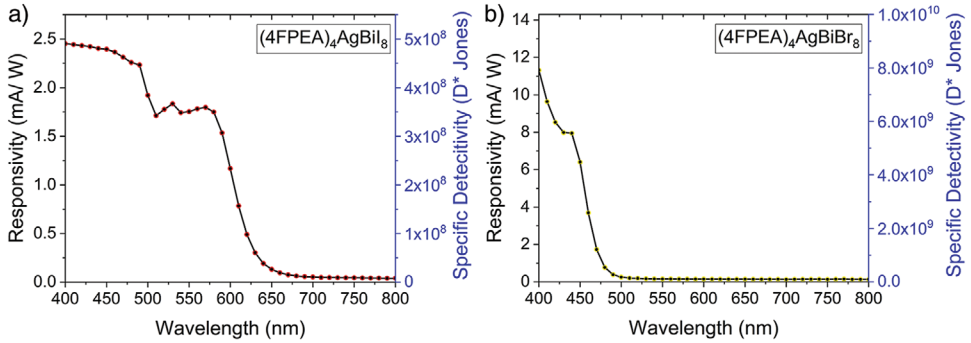

Figure 11. Responsivity and specific detectivity of photodetectors of a) $(4FPEA)_4AgBiI_8$ and b) $(4FPEA)_4AgBiBr_8$.

Therefore, we hypothesize that the lower OPTP signal and the observed ultrafast decay of the signal could imply ultrafast exciton formation rather than charge localization. These findings suggest that, while a significant fraction of free charge carriers contribute to the $(4FPEA)_4AgBiI_8$ excited state dynamics, the formation of excitons could rule the charge-carrier dynamics for $(4FPEA)_4AgBiBr_8$ when excited at 3.1 eV. However, we envision that further studies are needed to further investigate the difference between different halides.

Overall, our findings agree with the current interpretation of the charge-carrier dynamics, displaying much more complicated, underlying photophysical processes compared to 3D lead perovskites, because charge carriers are almost exclusively present as excitonic pairs, subsequently forming polarons as a result of the inherent spatial localization on the Ag-Bi based octahedra in the double perovskite structure, as well as structural reorganization following excitation which supports small-polaron formation.

2.5. Photodetectors

2D hybrid perovskites have been implemented successfully in various optoelectronic applications such as solar cells, field-effect transistors, X-ray- and photodetectors or light-emitting diodes.[24,32,36,68,69] Specifically, 2D Pb- and Sn-based perovskite photodetectors display excellent performance in terms of photoresponsivity and detectivity. However, their toxicity and environmental instability may limit their practical applications.[6] Some of the emerging lead-free 2D double perovskites have been demonstrated as phototransistors and polarized-light detectors.[24,48,68,70] Recently an Ag–Bi-based 2D double perovskite crystal $(iPA)_2CsAgBiBr_7$ has been demonstrated as an electronic device with a polarized light sensitivity application.[27] Another recent work demonstrated the high performance of a photodetector based on single-crystalline microwire arrays of $(R/S\text{-}\beta\text{-}MPA)_4AgBiI_8$ after employing a capillary-bridge assembly technique. While photodetectors based on bulk single crystal $(R/S\text{-}\beta\text{-}MPA)_4AgBiI_8$ achieved detectivities of 1.2×10^7 Jones, the incorporation into the microwire arrays achieved an increase of detectivity of up to 3.98×10^{11} Jones, demonstrating the importance of crystal quality, crystal orientation with regard to the electrode as well as the distance of the electrodes (single crystal channel area of 0.32 mm^2 compared to microwire channel width of 2 μm × height of 0.225 μm).[48,71]

Here, we demonstrate the first thin film, solution-processed Ag–Bi-based 2D double perovskite photodetectors fabricated via a one-step processing method. The air-stable solutions of $(4FPEA)_4AgBiBr_8$ and $(4FPEA)_4AgBiI_8$ are compatible with deposition protocols such as spin coating, doctor-blading, and drop casting, showing promise regarding scalable methods such as printing. The solutions for the devices can be prepared by directly dissolving the perovskite material, or dissolving the halide salts, as explained in the experimental section. The solutions were deposited on interdigitated gold electrodes (channel width of 10 μm) either by doctor blading or drop casting and were annealed at 80 °C for 5 min directly afterward. Since the photoconductivity setup was operated with a halogen lamp operating from 400 nm which is not sufficient for the excitation of the large band gap perovskite $(4FPEA)_4AgBiCl_8$, only the responsivity and specific detectivity of $(4FPEA)_4AgBiBr_8$ and $(4FPEA)_4AgBiI_8$ were characterized (**Figure 11**). A current–voltage measurement applied between 0 and 1 V provided a linear dependence for both materials, corresponding to an ohmic behavior with high resistance. At constant bias illumination with white light and an intensity of 100 mW cm^{-2} the current increased by a factor of three. The photodetectors based on $(4FPEA)_4AgBiI_8$ show responsivities of over 2 mA W^{-1} with a bias voltage of 1 V with a low noise level (110 pA Hz^{-1}), which results in a specific detectivity of up to 5×10^8 Jones (see Figure S29, Supporting Information). Photodetectors based on $(4FPEA)_4AgBiBr_8$ show higher responsivities of up to 10 mA W^{-1}, with a similar noise level and a specific detectivity of up to 6×10^9 Jones. A comparison with state-of-the-art lead-free perovskite photodetectors is given in Table S6, Supporting Information (see Figure S30, Supporting Information). Our devices based on $(4FPEA)_4AgBiI_8$ demonstrate a detectivity one order of magnitude higher than that based on bulk single crystal $(R/S\text{-}\beta\text{-}MPA)_4AgBiI_8$, but 3 orders of magnitude lower than those based on single crystalline microwire array $(R/S\text{-}\beta\text{-}MPA)_4AgBiI_8$.[48,71] We assume that the lower performance of the single-crystal-based device is caused by the top evaporated contacts, which should limit the out-of-plane charge transport and thus throughout the crystal, owing to the layered 2D structure and the insulating organic layers. This is partially overcome by using interdigitated contacts (i.e. microwire arrays). The crystallization method of a functionalized morphology to

control the capillary spread employed in the microwire arrays further increases the contact quality over the simple synthesis technique we employed here. Lastly, smaller channel widths or electrode distances seem to contribute to a better charge transport, because of the ultra-short lifetimes and large binding energies of the generated charge carriers in these materials. Although the 2D double perovskites show some intrinsic deficits compared to 3D Sn- and Ag-Bi-based perovskites, their incipient performance is already comparable, demonstrating the potential of controlled crystallization and orientational freedom intrinsic to 2D structures. Lastly, both devices have shown stable performance for more than two weeks with measurements and storage under ambient conditions.

3. Conclusion

We demonstrate the synthesis of three new 2D hybrid silver-bismuth double perovskites $(4FPEA)_4AgBiX_8$ (X = Cl, Br, I) and prove the ability of a simple, fluorinated organic spacer to stabilize the silver-bismuth-iodide double perovskite lattice. The simple solution-based synthesis yields highly crystalline materials in both bulk and thin-film form. The thin films crystallize as highly oriented structures in which organic and inorganic layers are oriented exclusively horizontally to the substrate surface. The crystalline thin-film quality can be tuned through choice of substrate and synthesis parameters to form domains of up to hundreds of microns with single-crystalline-grade morphology and orientation. DFT calculations reveal key properties such as the direct band gap caused by dimensional reduction. Moreover, we show how the band dispersion is influenced by the halides and attribute this to the growing degeneracy of the organic HOMO and inorganic VB from Cl to Br and I. Our temperature-dependent PL measurements show extremely broad and strongly Stokes shifted emission for all three materials. OPTP measurements point toward photoexcitation being followed by an initial, ultrafast charge-carrier localization and the formation of small-polaron states. We are thus able to account for the observed charge-carrier dynamics and emissive behavior through a mechanism based on inherent exciton formation, small-polaron formation (or "self-trapping") and defect-mediated recombination. Finally, we demonstrate the incorporation of $(4FPEA)_4AgBiBr_8$ and $(4FPEA)_4AgBiI_8$ into photodetector devices showing promising performance, if the interplay of intrinsic 2D double perovskite properties and morphological control for device fabrication is considered. Our work provides detailed insights into the emerging structural class of lead-free 2D hybrid double perovskites and their distinct properties in comparison to 3D double perovskite structures.

4. Experimental Section

Bulk and Single Crystals: 4-Fluorophenethylammonium salts (4FPEA*X*, X = Cl, Br, I) were synthesized by dissolving 1 eq. 4-fluorophenethylamine (Sigma–Aldrich 99%) in 150 mL ethanol (Fischer Scientific absolute, >99%) at 0 °C. Then, 1.1 eq. conc. H*X* acid (X = Cl, Br, I) (Sigma–Aldrich hydrochloric acid 37 wt% in H_2O, 99.999% trace metals basis; Sigma–Aldrich hydrobromic acid, 48 wt% in H_2O, ≥ 99.99%, 48%; Sigma–Aldrich hydroiodic acid 57 wt% in H_2O, distilled, stabilized, 99.95%) was slowly added and the mixture was stirred at 0 °C for 2 h. Afterward, the solution was allowed to warm up to room temperature and the solvent was removed under vacuum. The product was washed three times with adequate amounts of diethyl ether (Sigma–Aldrich contains 1 ppm BHT as inhibitor, anhydrous, ≥ 99.7%) and dried under medium vacuum.

Powders of $(4FPEA)_4AgBiX_8$ (X = Cl, Br, and I) were synthesized by slowly adding an excess of aq. conc. H*X* acid (X = Cl, Br, and I) (Sigma–Aldrich hydrochloric acid 37 wt% in H2O, 99.999% trace metals basis; Sigma–Aldrich hydrobromic acid, 48 wt% in H2O, ≥99.99%, 48%; Sigma–Aldrich hydroiodic acid 57 wt% in H_2O, distilled, stabilized, 99.95%) to 0.5 eq. Ag_2O (Fluka 99%), 0.5 eq. Bi_2O_3 (Alfa-Aesar 99,975% metals basis) and 4 eq. 4-fluorophenethylamine (Sigma–Aldrich 99%) under stirring at room temperature for 1 h. The solutions were filtered and the products were washed three times with adequate amounts of diethyl ether (Sigma–Aldrich contains 1 ppm BHT as an inhibitor, anhydrous, ≥99.7%) and then dried under medium vacuum.

Single crystals of $(4FPEA)_4AgBiBr_8$ were grown by dissolving the synthesized powder (as described above) in 1 mL GBL (γ-butyrolactone; Sigma–Aldrich ReagentPlus, ≥99%) in a small vial (V = 1.5 ml) which was placed in a bigger vial (V = 25 mL) filled with 2 ml dIPE (di-isopropylether; Sigma–Aldrich anhydrous, 99%). By vapor diffusion of the antisolvent dIPE into the GBL perovskite solution, single crystals were obtained and washed three times with adequate amounts of diethyl ether and dried under a medium vacuum.

Single crystals of $(4FPEA)_4AgBiI_8$ were grown by cooling a saturated aqueous HI solution with 1 eq. AgI (Sigma–Aldrich 99%), 1 eq. BiI_3 (TCI anhydrous) and 4 eq. 4FPEAI at 3° C h^{-1} from 110 to 30 °C. The solution was filtered and the obtained single crystals were washed three times with adequate amounts of diethyl ether and dried under medium vacuum.

Thin Films: The substrates FTO-coated glass, ITO-coated glass and Si–SiO_2 (polished with 300 nm thermally grown SiO_2) wafers were cleaned by ultrasonication for 15 min in a solution of acetone, isopropanol, and ethanol (1:1:1). Afterward, the substrates were cleaned for 10 min under nitrogen plasma. Stoichiometric amounts of AgX, BiX_3, and 4FPEAX (X = Cl, Br, I) (AgCl Sigma–Aldrich 99%; $BiCl_3$ Sigma–Aldrich > 98%; AgBr Alfa–Aesar 99,5%; $BiBr_3$ Sigma–Aldrich > 98%; AgI Sigma–Aldrich 99%; BiI_3 (TCI anhydrous > 98%) were dissolved in 1-methyl-2-pyrrolidinone (NMP Sigma–Aldrich anhydrous, 99.5%). Thin films on FTO and ITO were spin-coated in a glove box with N_2 atmosphere from a 0.5 M solution, thin films on Si–SiO_2 wafers were spin-coated from a 0.06 M solution. Thin films were spin-coated at an initial step of 3000 rpm for 10 s with a second step of 6000 rpm (FTO, ITO) or 8000 rpm (Si–SiO_2) for 50 s. The films were annealed at 100 °C for 3 min or 140 °C for 1 min with a subsequent annealing at 70 °C for 5 min to afford a slow cool down to room temperature.

Photodetectors: Gold contacts were prepared on glass substrates by optical lithography and thermal evaporation followed by a lift-off process. The electrodes are films of Au/Ti with 40/10 nm thickness. The size of the gap between electrodes was 10 µm and the total length was 8 mm, giving an 8×10^{-8} m^2 active area. The noise characterization was done with a larger active area of 0.1 cm^2. Photodetectors were fabricated by doctor blading or drop casting $(4FPEA)_4AgBiX_8$ (X = Br & I) solution in NMP onto prepatterned finger-structured gold contacts. The devices were then dried at 80 °C for 5 min at ambient conditions.

Characterization Techniques: *Powder X-Ray Diffraction (P-XRD)*: P-XRD measurements were carried out on a Stoe Stadi P diffractometer in Debye–Scherrer geometry, operating at 40 kV and 40 mA, using monochromated (Ge(111) single crystal monochromator) Cu-$K_{\alpha 1}$ radiation (λ = 1.5406 Å) and a Dectris Mythen 1k detector.

Thin Film X-Ray Diffraction (TF-XRD): TF-XRD measurements were carried out on a Bruker D8 Discover diffractometer in Bragg–Brentano geometry, with Ni-filtered Cu-$K_{\alpha 1}$ radiation (λ = 1.5406 Å) and a position-sensitive LynxEye detector.

Single-Crystal X-Ray Diffraction (SC-XRD): SC-XRD measurements were carried out on a Bruker D8 Venture Txs system equipped with a multilayer mirror monochromator and a Mo-K_α rotating anode X-ray tube (λ = 0.71073 Å). The frames were integrated with the Bruker SAINT software package. Data were corrected for absorption effects using the Multi-Scan method (SADABS). The structure was solved and refined using the Bruker Shelxtl Software Package.

Grazing-Incidence Wide Angle X-Ray Scattering (GIWAXS): GIWAXS measurements were carried out on an Anton-Paar Saxspoint 2.0 with a Primux 100 microfocus source with Cu-$K_{\alpha 1}$ radiation (λ = 1.5406 Å) and a Dectris Eiger R 1M 2D Detector.

Scanning Electron Microscopy (SEM) and Energy Dispersive X-Ray Spectroscopy (EDX): SEM and EDX measurements were carried out on a FEI Helios NanoLab G3 UC Dual Beam microscope.

Atomic Force Microscopy (AFM): AFM measurements were performed under ambient conditions using a Nanoink atomic force microscope with Si n-type tip with a radius of<10 nm in tapping mode with a scan rate of 0.2 Hz.

First-Principles Calculations Density-Functional Theory (DFT): First-principles DFT calculations were based on a plane wave basis set and pseudopotentials as implemented in the Quantum Espresso package.[72] Furthermore, the PBE exchange–correlation functional and the Tkatchenko–Scheffler (TS) dispersion scheme were used.[73,74] The latter is necessary to accurately describe the structural properties in low-dimensional perovskite materials.[75] The structures were optimized until all residual forces on the nuclei were below 1.0×10^{-3} a.u. Hereby, the following equilibrium unit cell parameters were obtained, all within less than 1% deviation from experimental data:

$$(4FPEA)_4AgBiI_8: \; a = 8.62, b = 8.75, c = 16.37, \; \alpha = 98.97, \beta = 90.12, \gamma = 90.01 \quad (1)$$

$$(4FPEA)_4AgBiBr_8: a = 7.83, b = 7.62, c = 30.22, \; \alpha = 90.00, \beta = 91.87, \gamma = 90.00 \quad (2)$$

$$(4FPEA)_4AgBiCl_8: a = 8.16, b = 7.78, c = 16.77, \; \alpha = 90.01, \beta = 97.38, \gamma = 90.12 \quad (3)$$

A kinetic energy cutoff of 50 Ry for the wavefunctions and 400 Ry for the charge density was used. For the bromide structure, a minimal, suitably converged $2 \times 2 \times 1$ k-point grid was utilized for SCF and relaxation calculations because of the large dimension of the system. The iodide and chloride compounds were calculated by using a larger $4 \times 4 \times 1$ grid. Furthermore, larger $12 \times 12 \times 3$ grids were used for NSCF calculations to accurately describe the projected DOS.

UV-Vis Absorption (UV-Vis): UV-Vis spectra were taken on a Perkin–Elmer Lambda 1050 spectrometer equipped with a 150 mm integration sphere. Thin films were measured in transmittance and reflectance mode. Powder measurements were measured in reflection mode with a Praying Mantis diffuse reflection setup.

Photoluminescence (PL): Photoluminescence spectra were measured with a self-built confocal microscope system. The used objective was a Nikon 100×0.75NA DIC with a working distance of 4 mm. Furthermore, a closed cycle cryostat system (Atto Dry 800, Attocube) with an ultra-short-working-distance option (3 mm from sample to outside) was installed, which allows one to control the sample temperature from 5 to 300 K. As laser-source for excitation a 405 nm pulsed laser diode (Pico Quant P-C-405) was used, which has an adjustable repetition rate and a pulse length of 50 to 300 ps, depending on the applied diode voltage. Besides, a Short Pass Filter 450 (Fesh 450 Thorlabs) in the excitation path was installed to clean the laser spectrum and a Long Pass Filter 490 (Chroma) was used for the detection side. In the detection path, an Avalanche Photo Diode (APD, model MPD PDM, 50 µm detector size) was built in for confocal images and was combined with a Time Correlated Single Photon Counting (TCSPC)-Card (Becker & Hickel) measuring time-dependent PL-decays. In addition, a second optical path was implemented with an Andor Shamrock spectrometer SR303i combined with a charged coupled device (CCD) camera (Andor Newton DU920 open electrode) to record spectra.

Photoconductivity (PC): Photoconductivity was measured by illumination with a tungsten lamp monochromatized through an Acton SP2150 (Princeton Instruments) spectrograph/monochromator. PC spectra were recorded for light modulated by a mechanical chopper with a frequency of 13 Hz. Bias was applied by a Keithley 236 SMU at 2 V, chosen according to the stability of the dark current. The signal was recorded by a Signal Recovery 7265 DSP lock-in amplifier, which provides as a standard output also the noise voltage or current per bandwidth. The setup was controlled by home-written software in LabView IV.

Optical-Pump Terahertz-Probe Spectroscopy: Our optical pump terahertz probe (OPTP) setup has been described in detail previously.[64] Briefly, the OPTP setup used an amplified Ti:sapphire laser system (Spitfire), providing 800-nm emission with 35 fs pulse duration and 5 kHz repetition rate. The fundamental output was used to generate single-cycle THz radiation pulses via the inverse spin Hall effect.[76] THz transmission was measured by using free-space electro-optic (EO) sampling with a 1 mm thick ZnTe (110) crystal, a Wollaston prism and a pair of balanced photodiodes. Samples for OPTP were deposited onto 2 mm thick *z*-cut quartz. In the setup, samples were excited by frequency-doubled 400 nm pulses, obtained by second-harmonic generation in a beta-barium-borate (BBO) crystal. During the OPTP measurements, the THz emitter, EO crystal, and samples were kept under vacuum at pressures below 0.1 mbar.

Crystal Structure Data: [CCDC 2151233–2151234 contains the supplementary crystallographic data for this paper. These data can be obtained free of charge from The Cambridge Crystallographic Data Centre via www.ccdc.cam.ac.uk/data_request/cif.]

Supporting Information

Supporting Information is available from the Wiley Online Library or from the author.

Acknowledgements

The authors thank Dr. Steffen Schmidt for the SEM and EDX measurements. The authors thank Dr. Peter Mayer for the SC-XRD measurements and structure solutions. Furthermore, the authors thank the Bavarian research network Solar Technologies go Hybrid, the Deutsche Forschungsgemeinschaft (DFG) Excellence Cluster e-conversion (EXC 2089/1 – 390776260) and the DFG focus program SPP 2196 for funding. L.M.H. acknowledges support through a Hans Fischer Senior Fellowship from the Technical University of Munich's Institute for Advanced Study, funded by the German Excellence Strategy.

Open access funding enabled and organized by Projekt DEAL.

Conflict of Interest

The authors declare no conflict of interest.

Data Availability Statement

The data that support the findings of this study are available from the corresponding author upon reasonable request.

Keywords

2D double perovskites, charge-carrier dynamics, oriented thin-films, photodetectors, silver-bismuth

Received: February 14, 2022
Revised: May 18, 2022
Published online:

[1] S. D. Stranks, H. J. Snaith, *Nat. Nanotechnol.* **2015**, *10*, 391.
[2] W. Yu, F. Li, L. Yu, M. R. Niazi, Y. Zou, D. Corzo, A. Basu, C. Ma, S. Dey, M. L. Tietze, U. Buttner, X. Wang, Z. Wang, M. N. Hedhili, C. Guo, T. Wu, A. Amassian, *Nat. Commun.* **2018**, *9*, 5354.
[3] L. Yin, H. Wu, W. Pan, B. Yang, P. Li, J. Luo, G. Niu, J. Tang, *Adv. Opt. Mater.* **2019**, *7*, 1900491.
[4] A. Sadhanala, S. Ahmad, B. Zhao, N. Giesbrecht, P. M. Pearce, F. Deschler, R. L. Hoye, K. C. Gödel, T. Bein, P. Docampo, *Nano Lett.* **2015**, *15*, 6095.
[5] A. H. Slavney, T. Hu, A. M. Lindenberg, H. I. Karunadasa, *J. Am. Chem. Soc.* **2016**, *138*, 2138.
[6] Y. Zhang, Y. Ma, Y. Wang, X. Zhang, C. Zuo, L. Shen, L. Ding, *Adv. Mater.* **2021**, *33*, e2006691.
[7] G. Meyer, *Prog. Solid State Chem.* **1982**, *14*, 141.
[8] N. Elliott, L. Pauling, *J. Am. Chem. Soc.* **1938**, *60*, 1846.
[9] E. T. McClure, M. R. Ball, W. Windl, P. M. Woodward, *Chem. Mater.* **2016**, *28*, 1348.
[10] H. C. Sansom, G. Longo, A. D. Wright, L. R. V. Buizza, S. Mahesh, B. Wenger, M. Zanella, M. Abdi-Jalebi, M. J. Pitcher, M. S. Dyer, T. D. Manning, R. H. Friend, L. M. Herz, H. J. Snaith, J. B. Claridge, M. J. Rosseinsky, *J. Am. Chem. Soc.* **2021**, *143*, 3983.
[11] Z. Deng, F. Wei, S. Sun, G. Kieslich, A. K. Cheetham, P. D. Bristowe, *J. Mater. Chem. A* **2016**, *4*, 12025.
[12] T. T. Tran, J. R. Panella, J. R. Chamorro, J. R. Morey, T. M. McQueen, *Mater. Horiz.* **2017**, *4*, 688.
[13] G. Volonakis, A. A. Haghighirad, R. L. Milot, W. H. Sio, M. R. Filip, B. Wenger, M. B. Johnston, L. M. Herz, H. J. Snaith, F. Giustino, *J. Phys. Chem. Lett.* **2017**, *8*, 772.
[14] B. A. Connor, R.-I. Biega, L. Leppert, H. I. Karunadasa, *Chem. Sci.* **2020**, *11*, 7708.
[15] M. Roknuzzaman, J. A. Alarco, H. Wang, K. Ostrikov, *Comput. Mater. Sci.* **2021**, *186*, 110009.
[16] F. Wei, Z. Deng, S. Sun, F. Xie, G. Kieslich, D. M. Evans, M. A. Carpenter, P. D. Bristowe, A. K. Cheetham, *Mater. Horiz.* **2016**, *3*, 328.
[17] W. Pan, H. Wu, J. Luo, Z. Deng, C. Ge, C. Chen, X. Jiang, W.-J. Yin, G. Niu, L. Zhu, L. Yin, Y. Zhou, Q. Xie, X. Ke, M. Sui, J. Tang, *Nat. Photonics* **2017**, *11*, 726.
[18] O. A. Lozhkina, A. A. Murashkina, M. S. Elizarov, V. V. Shilovskikh, A. A. Zolotarev, Y. V. Kapitonov, R. Kevorkyants, A. V. Emeline, T. Miyasaka, *Chem. Phys. Lett.* **2018**, *694*, 18.
[19] D. Bartesaghi, A. H. Slavney, M. C. Gelvez-Rueda, B. A. Connor, F. C. Grozema, H. I. Karunadasa, T. J. Savenije, *J. Phys. Chem. C* **2018**, *122*, 4809.
[20] E. Greul, Michiel, L. Petrus, A. Binek, P. Docampo, T. Bein, *J. Mater. Chem. A* **2017**, *5*, 19972.
[21] M. T. Sirtl, F. Ebadi, B. T. Gorkom, P. Ganswindt, R. A. J. Janssen, T. Bein, W. Tress, *Adv. Opt. Mater.* **2021**, *9*, 2100202.
[22] M. T. Sirtl, M. Armer, L. K. Reb, R. Hooijer, P. Dörflinger, M. A. Scheel, K. Tvingstedt, P. Rieder, N. Glück, P. Pandit, S. V. Roth, P. Müller-Buschbaum, V. Dyakonov, T. Bein, *ACS Appl. Energy Mater.* **2020**, *3*, 11597.
[23] B. A. Connor, L. Leppert, M. D. Smith, J. B. Neaton, H. I. Karunadasa, *J. Am. Chem. Soc.* **2018**, *140*, 5235.
[24] X. Wang, K. Li, H. Xu, N. Ali, Y. Wang, Q. Shen, H. Wu, *Chem. Commun.* **2020**, *56*, 7917.
[25] M. T. Sirtl, R. Hooijer, M. Armer, F. G. Ebadi, M. Mohammadi, C. Maheu, A. Weis, B. T. van Gorkom, S. Häringer, R. A. J. Janssen, T. Mayer, V. Dyakonov, W. Tress, T. Bein, *Adv. Energy Mater.* **2022**, *12*, 2103215.
[26] M. Pantaler, V. Diez-Cabanes, V. I. E. Queloz, A. Sutanto, P. A. Schouwink, M. Pastore, I. García-Benito, M. K. Nazeeruddin, D. Beljonne, D. C. Lupascu, C. Quarti, G. Grancini, *JACS Au* **2021**, *2*, 136.
[27] Y. Li, T. Yang, Z. Xu, X. Liu, X. Huang, S. Han, Y. Liu, M. Li, J. Luo, Z. Sun, *Angew. Chem., Int. Ed. Engl.* **2020**, *59*, 3429.
[28] L. Mao, S. M. L. Teicher, C. C. Stoumpos, R. M. Kennard, R. A. DeCrescent, G. Wu, J. A. Schuller, M. L. Chabinyc, A. K. Cheetham, R. Seshadri, *J. Am. Chem. Soc.* **2019**, *141*, 19099.
[29] A. Walsh, *J. Phys. Chem. C* **2015**, *119*, 5755.
[30] Z. Xiao, W. Meng, J. Wang, Y. Yan, *ChemSusChem* **2016**, *9*, 2628.
[31] P. Vishnoi, R. Seshadri, A. K. Cheetham, *J. Phys. Chem. C* **2021**, *125*, 11756.
[32] Z. Xu, X. Liu, Y. Li, X. Liu, T. Yang, C. Ji, S. Han, Y. Xu, J. Luo, Z. Sun, *Angew. Chem., Int. Ed.* **2019**, *58*, 15757.
[33] Y. Yao, B. Kou, Y. Peng, Z. Wu, L. Li, S. Wang, X. Zhang, X. Liu, J. Luo, *Chem. Commun.* **2020**, *56*, 3206.
[34] M. K. Jana, S. M. Janke, D. J. Dirkes, S. Dovletgeldi, C. Liu, X. Qin, K. Gundogdu, W. You, V. Blum, D. B. Mitzi, *J. Am. Chem. Soc.* **2019**, *141*, 7955.
[35] F. Zhang, D. H. Kim, H. Lu, J. S. Park, B. W. Larson, J. Hu, L. Gao, C. Xiao, O. G. Reid, X. Chen, Q. Zhao, P. F. Ndione, J. J. Berry, W. You, A. Walsh, M. C. Beard, K. Zhu, *J. Am. Chem. Soc.* **2019**, *141*, 5972.
[36] J. Shi, Y. Gao, X. Gao, Y. Zhang, J. Zhang, X. Jing, M. Shao, *Adv. Mater.* **2019**, *31*, e1901673.
[37] W. Fu, H. Liu, X. Shi, L. Zuo, X. Li, A. K. Y. Jen, *Adv. Funct. Mater.* **2019**, *29*, 1900221.
[38] D. B. Straus, S. Hurtado Parra, N. Iotov, Q. Zhao, M. R. Gau, P. J. Carroll, J. M. Kikkawa, C. R. Kagan, *ACS Nano* **2020**, *14*, 3621.
[39] Y. Chen, Y. Sun, J. Peng, J. Tang, K. Zheng, Z. Liang, *Adv. Mater.* **2018**, *30*.
[40] R. G. Pearson, *J. Am. Chem. Soc.* **2002**, *91*, 4947.
[41] J. A. McMillan, *J. Inorge. Nucl. Chem.* **1960**, *13*, 28.
[42] D. B. Mitzi, *Inorg. Chem.* **2000**, *39*, 6107.
[43] L.-Y. Bi, Y.-Q. Hu, M.-Q. Li, T.-L. Hu, H.-L. Zhang, X.-T. Yin, W.-X. Que, M. S. Lassoued, Y.-Z. Zheng, *J. Mater. Chem. A* **2019**, *7*, 19662.
[44] D. Fu, S. Wu, Y. Liu, Y. Yao, Y. He, X.-M. Zhang, *Inorg. Chem. Front.* **2021**, *8*, 3576.
[45] X. Li, B. Traoré, M. Kepenekian, L. Li, C. C. Stoumpos, P. Guo, J. Even, C. Katan, M. G. Kanatzidis, *Chem. Mater.* **2021**, *33*, 6206.
[46] Z. Xu, H. Wu, D. Li, W. Wu, L. Li, J. Luo, *J. Mater. Chem. C* **2021**, *9*, 13157.
[47] M. S. Lassoued, L.-Y. Bi, Z. Wu, G. Zhou, Y.-Z. Zheng, *J. Mater. Chem. C* **2020**, *8*, 5349.
[48] Y. Zhao, M. Dong, J. Feng, J. Zhao, Y. Guo, Y. Fu, H. Gao, J. Yang, L. Jiang, Y. Wu, *Adv. Opt. Mater.* **2021**, *10*, 2102227.
[49] F. Schmitz, J. Horn, N. Dengo, A. E. Sedykh, J. Becker, E. Maiworm, P. Belteky, A. Kukovecz, S. Gross, F. Lamberti, K. Muller-Buschbaum, D. Schlettwein, D. Meggiolaro, M. Righetto, T. Gatti, *Chem. Mater.* **2021**, *33*, 4688.
[50] E. Brandes, W. Möller, M. Molnárné, T. Schendler, V. Schröder, *Sicherheitstechnische Kenngrößen*, Wirtschaftsverlag NW, Verlag für neue Wissenschaft, **2003**.
[51] J. Su, T. Mou, J. Wen, B. Wang, *J. Phys Chem. C* **2020**, *124*, 5371.
[52] P. J. Hasnip, K. Refson, M. I. Probert, J. R. Yates, S. J. Clark, C. J. Pickard, *Philos. Trans. R. Soc., A* **2014**, *372*, 20130270.
[53] C. Liu, W. Huhn, K. Z. Du, A. Vazquez-Mayagoitia, D. Dirkes, W. You, Y. Kanai, D. B. Mitzi, V. Blum, *Phys. Rev. Lett.* **2018**, *121*, 146401.
[54] P. Kubelka, F. Munk, *Z. Tech. Phys.* **1931**, *12*, 259.
[55] A. D. Wright, L. R. V. Buizza, K. J. Savill, G. Longo, H. J. Snaith, M. B. Johnston, L. M. Herz, *J. Phys. Chem. Lett.* **2021**, *12*, 3352.
[56] J. C. Blancon, A. V. Stier, H. Tsai, W. Nie, C. C. Stoumpos, B. Traore, L. Pedesseau, M. Kepenekian, F. Katsutani, G. T. Noe, J. Kono, S. Tretiak, S. A. Crooker, C. Katan, M. G. Kanatzidis, J. J. Crochet, J. Even, A. D. Mohite, *Nat. Commun.* **2018**, *9*, 2254.

[57] R. I. Biega, M. R. Filip, L. Leppert, J. B. Neaton, *J. Phys. Chem. Lett.* **2021**, *12*, 2057.
[58] R. Kentsch, M. Scholz, J. Horn, D. Schlettwein, K. Oum, T. Lenzer, *J. Phys. Chem. C* **2018**, *122*, 25940.
[59] T. Hu, M. D. Smith, E. R. Dohner, M. J. Sher, X. Wu, M. T. Trinh, A. Fisher, J. Corbett, X. Y. Zhu, H. I. Karunadasa, A. M. Lindenberg, *J. Phys. Chem. Lett.* **2016**, *7*, 2258.
[60] J. A. Steele, P. Puech, M. Keshavarz, R. Yang, S. Banerjee, E. Debroye, C. W. Kim, H. Yuan, N. H. Heo, J. Vanacken, A. Walsh, J. Hofkens, M. B. J. Roeffaers, *ACS Nano* **2018**, *12*, 8081.
[61] A. D. Wright, C. Verdi, R. L. Milot, G. E. Eperon, M. A. Perez-Osorio, H. J. Snaith, F. Giustino, M. B. Johnston, L. M. Herz, *Nat. Commun.* **2016**, *7*, 1.
[62] C. Wehrenfennig, G. E. Eperon, M. B. Johnston, H. J. Snaith, L. M. Herz, *Adv. Mater.* **2014**, *26*, 1584.
[63] M. Righetto, D. Giovanni, S. S. Lim, T. C. Sum, *Appl. Phys. Rev.* **2021**, *8*, 011318.
[64] L. R. V. Buizza, A. D. Wright, G. Longo, H. C. Sansom, C. Q. Xia, M. J. Rosseinsky, M. B. Johnston, H. J. Snaith, L. M. Herz, *ACS Energy Lett.* **2021**, *6*, 1729.
[65] H. Hempel, T. J. Savenjie, M. Stolterfoht, J. Neu, M. Failla, V. C. Paingad, P. Kužel, E. J. Heilweil, J. A. Spies, M. Schleuning, J. Zhao, D. Friedrich, K. Schwarzburg, L. D. A. Siebbeles, P. Dörflinger, V. Dyakonov, R. Katoh, M. J. Hong, J. G. Labram, M. Monti, E. Butler-Caddle, J. Lloyd-Hughes, M. M. Taheri, J. B. Baxter, T. J. Magnanelli, S. Luo, J. M. Cardon, S. Ardo, T. Unold, *Adv. Energy Mater.* **2022**, *12*, 2102776.
[66] D. H. Fabini, R. Seshadri, M. G. Kanatzidis, *MRS Bull.* **2020**, *45*, 467.
[67] Z. Xiao, W. Meng, J. Wang, D. B. Mitzi, Y. Yan, *Mater. Horiz.* **2017**, *4*, 206.
[68] M. Li, S. Han, B. Teng, Y. Li, Y. Liu, X. Liu, J. Luo, M. Hong, Z. Sun, *Adv. Opt. Mater.* **2020**, *8*, 2000149.
[69] L. Zhu, D. Liu, J. Wang, N. Wang, *J. Phys. Chem. Lett.* **2020**, *11*, 8502.
[70] C. Chen, L. Gao, W. Gao, C. Ge, X. Du, Z. Li, Y. Yang, G. Niu, J. Tang, *Nat. Commun.* **2019**, *10*, 1927.
[71] D. Li, X. Liu, W. Wu, Y. Peng, S. Zhao, L. Li, M. Hong, J. Luo, *Angew. Chem., Int. Ed. Engl.* **2021**, *60*, 8415.
[72] P. Giannozzi, S. Baroni, N. Bonini, M. Calandra, R. Car, C. Cavazzoni, D. Ceresoli, G. L. Chiarotti, M. Cococcioni, I. Dabo, *J. Phys. Condens. Matter* **2009**, *21*, 395502.
[73] J. P. Perdew, K. Burke, M. Ernzerhof, *Phys. Rev. Lett.* **1996**, *77*, 3865.
[74] A. Tkatchenko, M. Scheffler, *Phys. Rev. Lett.* **2009**, *102*, 073005.
[75] R. L. Z. Hoye, P. Schulz, L. T. Schelhas, A. M. Holder, K. H. Stone, J. D. Perkins, D. Vigil-Fowler, S. Siol, D. O. Scanlon, A. Zakutayev, A. Walsh, I. C. Smith, B. C. Melot, R. C. Kurchin, Y. Wang, J. Shi, F. C. Marques, J. J. Berry, W. Tumas, S. Lany, V. Stevanović, M. F. Toney, T. Buonassisi, *Chem. Mater.* **2017**, *29*, 1964.
[76] T. Seifert, S. Jaiswal, U. Martens, J. Hannegan, L. Braun, P. Maldonado, F. Freimuth, A. Kronenberg, J. Henrizi, I. Radu, E. Beaurepaire, Y. Mokrousov, P. M. Oppeneer, M. Jourdan, G. Jakob, D. Turchinovich, L. M. Hayden, M. Wolf, M. Münzenberg, M. Kläui, T. Kampfrath, *Nat. Photonics* **2016**, *10*, 483.